DELFT UNIVERSITY OF TECHNOLOGY

MASTER THESIS

Modeling MIC and Metal Precipitation with a 1D Reactive Transport Model

Jianchao Zhou

Student number: 4316150

MSc Applied Earth Science

Track: Geo-Engineering

TU Delft Delft University of Technology

The people who have provide aid and evaluate the process are:

Prof. dr. ir. T. J. Heimovaara (Chairman)
Organization: Delft University of Technology
Faculty: Civil Engineering and Geosciences
Section: Geo-engineering
Address: Stevinweg 1, room KG 00.540
2628 CN Delft
E-mail: t.j.Heimovaara@tudelft.nl

Dr. P. J. Vardon
Organization: Delft University of Technology
Faculty: Civil Engineering and Geosciences
Section: Geo-engineering
Address: Stevinweg 1, room CT 00.490
2628 CN Delft
E-mail: P.J.Vardon@tudelft.nl

Dr. ir. M. Bakker
Organization: Delft University of Technology
Faculty: Civil Engineering and Geosciences
Section: Water Resources
Address: Stevinweg 1, room CT 4.92.1
2628 CN Delft
E-mail: mark.bakker@tudelft.nl

MSc. M. Afanasyev
Organization: Delft University of Technology
Faculty: Civil Engineering and Geosciences
Section: Geo-engineering
Address: Stevinweg 1, room CT 00.460
2628 CN Delft
E-mail: M.Afanasyev@tudelft.nl

MSc. A. van Turnhout
Organization: Delft University of Technology
Faculty: Civil Engineering and Geosciences
Section: Geo-engineering
Address: Stevinweg 1, room CT 00.460
2628 CN Delft
E-mail: A.G.vanTurnhout@tudelft.nl

Contents

1 Introduction **1**
1.1 Motivation . . . 1
1.2 Goals . . . 1
1.3 Thesis outlines . . . 2

2 Theory **3**
2.1 Microbially influenced corrosion . . . 3
2.1.1 Interactions between MIC and mineral precipitation . . . 3
2.1.1.1 Effects of galvanic cells on mineral precipitation . . . 3
2.1.1.2 Effects of acid attack on mineral precipitation . . . 4
2.2 Microbially influenced mineral precipitation . . . 4
2.3 Microbial activities . . . 5
2.3.1 Microbial growth system . . . 5
2.3.2 Biomass composition . . . 6
2.3.3 Biomass growth kinetics . . . 6
2.3.4 Energy-based maximum growth rate estimation . . . 7
2.3.5 Dominating bacteria in MIC . . . 8
2.3.5.1 Sulfate reducing bacteria . . . 9
2.3.5.2 Methanogens . . . 9
2.3.5.3 Competition among bacteria . . . 9
2.4 Chemical reactions . . . 10
2.4.1 Redox reaction . . . 10
2.4.1.1 Sequential utilization of electrons . . . 10
2.4.1.2 Degradation of organic electron donors . . . 12
2.4.2 Equilibrium reaction . . . 14
2.4.3 Mineral precipitation-dissolution . . . 15
2.4.4 Electrical neutrality . . . 17
2.5 Diffusion of reactants . . . 18
2.5.1 Porous medium properties changes . . . 18
2.5.1.1 Effects of solid mass accumulation on Φ . . . 18
2.5.1.2 Effects of solid mass accumulation on k_{ra} . . . 19
2.5.2 Diffusion of aqueous species . . . 19

3 Model development **21**
3.1 Model assumptions . . . 21
3.2 Existing reactive transport model evaluation . . . 21
3.3 Model structure . . . 22
3.3.1 Model components . . . 22
3.3.2 Coupling algorithm . . . 22
3.3.3 Implementation details . . . 24
3.3.3.1 Selection of reference states . . . 24
3.3.3.2 Single ORI versus multiple ORIs . . . 25

4 Model testing **26**
4.1 Microbially catalyzed urea hydrolysis 26
4.1.1 Experiments description 26
4.1.2 Numerical simulation 27
4.2 Calcite precipitation under double diffusion 29
4.3 Microbially influenced mineral precipitation 31
4.3.1 Varying boundary concentrations 31
4.3.2 Varying distances 34

5 Results and discussions **36**
5.1 Urea hydrolysis simulation 36
5.2 Calcite precipitation simulation 39
5.3 Microbially influenced mineral precipitation simulation 41
5.3.1 Varying boundary concentrations 42
5.3.1.1 Varying sulfate boundary concentrations 42
5.3.1.2 Varying iron corrosion rates 45
5.3.2 Effects of varying boundary concentrations 47
5.3.3 Varying distances 47
5.3.4 Effects of varying distances 49
5.4 Effects of varying precipitation rates 49

6 Summary and conclusions **51**

A Energy-based stoichiometry derivation **i**

B Gas formation and transfer **iii**
B.1 Pre-defined gas bubble solution iii
B.2 Unsaturated transport solution iv

List of Tables

2.1 Equilibria in the carbonic acid system with approximate equilibrium constant at 293.15 K (Appelo and Postma, 2005) 14
4.1 Initial conditions in the urea hydrolysis simulation 26
4.2 Reaction network in the microbially catalyzed urea hydrolysis experiment . . . 27
4.3 Parameters used in the urea hydrolysis simulation 28
4.4 Transport and discretization parameters used in the urea hydrolysis simulation . 29
4.5 Reaction network for c7uu experiment (Gebrehiwet, et al., 2014) 30
4.6 Boundary conditions used in the calcite precipitation simulation 30
4.7 Parameters used in the calcite precipitation simulation 30
4.8 Transport and discretization parameters used in this calcium precipitation simulation 31
4.9 Initial concentrations in microbially influenced mineral precipitation simulation 32
4.10 Summary of microbially influenced mineral precipitation numerical experiments 33
4.11 Reaction network of the microbially influenced mineral precipitation in the presence of SRB 34
4.12 Transport and discretization parameters used in the microbially influenced mineral precipitation simulation 34
4.13 Parameters used in the microbially influenced mineral precipitation simulation . 35
5.1 Measures of the pH limit progression (Provided by van Paassen) 36
A.1 Standard Gibbs energy of formation (Heijnen and Kleerebezem, 1999) i

List of Figures

2.1 Systematic description of MIC mechanisms (Copied from Usher, et al., 2014) . 3
2.2 Interpretation of microbially influenced mineral precipitation 4
2.3 Predication of mineral precipitation from local supersaturation degree (Copied from Gebrehiwet, et al., 2014) 5
2.4 Schematic definition of microbial growth (Copied from Heijnen and Kleerebezem, 1999) 6
2.5 Sequence of important redox processes at pH = 7 in natural system (Copied from Appelo and Postma, 2005; Stumm and Morgan, 1996) 11
2.6 Schematic pathway of organic matter decomposition under anaerobic conditions (Copied from Appelo and Postma, 2005) 13
2.7 The activities of CO_2 species in water at constant total inorganic carbon (Copied from Appelo and Postma, 2005) 15
2.8 Stability of iron minerals at 293.15 K. $TIC = 10^{-2.5}$. (Copied from Appelo and Postma, 2005) 17
3.1 Multiple ORI versus single ORI 25
4.1 Microbially catalyzed urea hydrolysis experimental set-up (Provided by van Paassen) 26
4.2 Estimated diffusion coefficient for 2.5% agar gel 28
4.3 Double diffusion configuration of calcium precipitation experiment (Copied from Gebrehiwet, et al., 2014) 29
4.4 Corrosion rate and ferrous iron concentration correlation (King et al., 1973) . . 32
5.1 Errors in color change measurement (Provided by van Paassen) 37
5.2 Comparison between experimental observation and model simulation result . . 37
5.3 Progress of urea hydrolysis (arrows indicate changes over time) 38
5.4 Simulated *pH* limit progression after 30 days 39
5.5 Simulation results and experimental observation for the calcite precipitation . . 40
5.6 Progress of calcite precipitation under double diffusion control (arrows indicate changes over time) 41
5.7 Solid mass accumulation and transport properties regarding various boundary sulfate concentrations after 30 days 42
5.8 Aqueous species profile regarding various boundary sulfate concentrations after 30 days 43
5.9 Progress of solid mass accumulation and transport properties changes in series S3 (arrows indicate changes over time) 44
5.10 Progress of aqueous species concentration changes in series S3 (arrows indicate changes over time) 44
5.11 Solid mass accumulation and transport properties regarding varying corrosion rates after 30 days 45
5.12 Aqueous species profile regarding varying corrosion rates after 30 days 46
5.13 *pH* development and carbonic acid speciation process in F3 series (arrows indicate changes over time) 46

5.14 Solid mass accumulation and transport properties regarding varying distances after 30 days 48
5.15 Aqueous species profile regarding varying distances after 30 days 48
5.16 Cumulative iron mineral precipitation in L series 49
5.17 The simulated calcite precipitation with various precipitation rates after 47 days 50
B.1 Schematic representation of gas bubble in the system iii

NOTATION

Symbol	Definition	Dimension
A	Temperature dependent constant	-
A_0	Initial surface area	dm^2
C_i^D	Derived concentration of compound i	mol L^{-1}
C_i	Concentration of compound i	mol L^{-1}
$C_{g,i}$	Gas concentration of component i	mol L^{-1}
$C_{ref,i}^T$	Total concentration of compound i in reference state	mol L^{-1}
D_i	Diffusion coefficient of component i	dm^2 d^{-1}
f_{cat}	Catabolism multiplication factor	-
f_i	Fraction of electron used by ith pathway	-
F	Formation factor	-
F_{out}	Amount of gas component i has been collected	mol d^{-1} L^{-1}
H_i	Henry's coefficient for component i	L atm mol^{-1}
I	Ionic strength	-
IAP	Ion activity product	-
k	Intrinsic permeability	L^2
k_1^i	Precipitation rate of mineral i	mol d^{-1} L^{-1}
k_2^i	Dissolution rate of mineral i	d^{-1}
k_{dec}	Constant decay rate	d^{-1}
$k_{La,i}$	Gas transfer rate for gas component i	d^{-1}
k_m	Specific mineral precipitation rate	d^{-1}
k_{ra}	Relative permeability	-
K_M	Solubility product	-
$K_{s,i}$	Affinity constant for ith compound	mol L^{-1}
L	Length of domain	m
$m_{0,i}$	Initial moles of solid i	mol
m_G	Gibbs energy production rate	kJ $mol^{-1}d^{-1}$
m_i	Molarity of ion i	mol L^{-1}
$m_{s,i}$	Moles of solid i at a given time	mol
M_i	Molar mass of compound i	g mol^{-1}
NoC	Carbon length	-
p	Gas partial pressure	atm
P_{air}	Partial gas pressure	Pa
P_c	Capillary pressure	Pa
P_{entry}	Entry pressure	Pa
P_{water}	Water pressure	Pa

Q^{α}	Sink term of fluid α	mol d^{-1} L^{-1}
$q_{D,i}$	Diffusive flux of compound i	m s^{-1}
q_e^{max}	Maximum biomass specific electron-transfer rate	d^{-1}
q_{α}	Flux vector of fluid α	m s^{-1}
R	Gas constant	L atm K^{-1} mol^{-1}
R_C	Total rate of organic carbon degradation	d^{-1}
$R_{e,i}$	Rate of carbon oxidation by the ith pathway	d^{-1}
$R_{i,in}$	Supply of gas component i from liquid phase	mol d^{-1} L^{-1}
$R_{m,i}$	Overall precipitation rate of mineral i	mol $L^{-1}d^{-1}$
S_i	Bio-chemical sink term	mol d^{-1} L^{-1}
S_{eff}	Effective saturation degree	-
S_{α}	Saturation degree of fluid α	-
t	Time	d
T	Temperature	K
T_L	Tortuosity	-
V	Volume of solution	L
x_i	Mass fraction of gas component i	-
X^s	Mass of microbial cells per unit mass of aquifer solids	-
Y^{ogr}	Biomass yield coefficient	mol cell-C mol OC^{-1}
Y_D^{an}	Stoichiometry of electron donor in anabolism	-
z_i	Charge number of ion i	-
α	Speciation factor	-
γ	Reduction degree	-
$\mu_{max,i}$	Maximum biomass growth rate of ith bacteria	d^{-1}
μ_{α}	Viscosity of fluid α	kg m^{-1} s^{-1}
ρ_i	Density of compound i	g cm^{-3}
ρ_{α}	Density of fluid α	g cm^{-3}
Υ_i	Activities coefficient of compound i	-
Ω_i	Saturation state of ith mineral	-
Φ	Porosity	-
$\triangle G_{Overall}^{min}$	Minimum Gibbs energy of dissipation	kJ mol^{-1}
$\triangle G_{cat}$	Gibbs energy changes of this catabolic reaction	kJ mol^{-1}
$\triangle G_{ana}$	Gibbs energy changes of this anabolic reaction	kJ mol^{-1}
$[EA_i]_{lim}$	Limiting concentration for electron acceptor i	mol L^{-1}

1 Introduction

1.1 Motivation

Corrosion of metals is a major issue in the subsurface environment. On the one hand, it causes enormous economic damage, according to the estimation conducted by Koch, et al., (2002), the annual cost of corrosion is approximately 276 billions dollars; on the other hand, it also alters the subsurface environment in various aspects. Corrosion in the subsurface environment is a complex process, it is the sum of multiple parallel or serial processes. Corrosion contains the electrochemical process which pertains to the oxidation of zero valent metals, the transport process accounting for the spatial migration of ionic metals and other byproducts and the biochemical interactions between the metallic surface and surrounding environment (Cole and Marney, 2012).

Beech and Gaylarde (1999) have concluded that biochemical processes can be dominant, especially when the microorganisms are in close contact with metallic surface. Microorganisms starts to develop when nutrients from the surrounding are available. Possible nutrients for microorganisms can be both organic and inorganic, for instance zero valent iron (Enning et al., 2012). According to Gorbushina (2007), the constant interplay between the surrounding and colonizers impacts on bio-geochemistry and microbial ecology. In terms of microbially influenced corrosion (MIC) and metal precipitation, the nutrients and energy consumption of microorganisms on the one hand affects the solid metal oxidation process (Usher et al., 2014); on the other hand the byproducts of metabolism are the reactants for metallic ions precipitation (Konhauser, 1997; Kjeldsen et al., 1998). Furthermore, formed solid mass including biomass and precipitated minerals is physically interconnected with the transport properties of porous medium (Pintelon et al., 2012; Bottero et al., 2013).

This research translates the microbially influenced solid metal oxidation into a constant metal dissolution rate, and aims at a comprehensive investigation on the microbially influenced mineral precipitation process regarding various environmental conditions via mathematical modeling. Environmental conditions are considered to have a dominant effects on the magnitude and position and width of precipitated minerals (Gebrehiwet, et al., 2014). With the aid of the model predication, a more comprehensive insight into the relations between the development of microbially influenced mineral precipitation and the environmental conditions can be obtained.

1.2 Goals

The goals of this research are 1) to implement the 1D reactive transport model which includes microbial activities, 2) to apply the developed model to obtain more insight into the microbially influenced mineral precipitation process.

The model is based on a reaction network with realistic rate relations, which is linked to the physical transport process occurring in a porous medium. With this model, it is possible to simulate any microbially related process in the subsurface environment.

The model is used to investigate the microbially influenced mineral precipitation process. This investigation mainly focuses on effect of the boundary substrate concentrations and the distance on the spatial and temporal distribution of precipitated minerals.

1.3 Thesis outlines

This thesis consists of six sections:

- Section 1 gives a systematic description of the framework of this research;
- Section 2 contains a literature review and the theoretical background is given;
- Section 3 focuses on the development of our model;
- Section 4 defines two scenarios with respect to various purposes. Scenario 1 is for verification, the model simulation is compared with urea hydrolysis experiment. Scenario 2 applies the model on a abiotic calcite precipitation simulation. Scenario 3 investigates the relationship between environmental conditions and microbially influenced mineral precipitation;
- Section 5 gives the results and discussions of scenarios simulations ;
- Section 6 draws the conclusions of this research.

2 Theory

2.1 Microbially influenced corrosion

Corrosion is an electrochemical process where metals were oxidized and the electrons released from the oxidation are used to reduce other chemical substances (Cole and Marney, 2012). Microbially influenced corrosion (MIC) is one corrosion that integrates the role of microbial activities into the process. MIC is a broad concept, with respect to specific metal oxidation mechanisms, it can be subdivided into more detailed mechanisms. Enning and Garrelfs (2014) studied biocorrosion induced by sulfate reducing bacteria (SRB), and they categorized MIC mechanisms into two main classes, EMIC (electrical microbially influenced corrosion) and CMIC (chemical microbially influenced corrosion). Meanwhile, Usher et al., (2014) focused on a more systematic description of MIC mechanisms as presented in Figure 2.1. They summarized that the major MIC mechanisms are acid attack, fixing anodic sites, formation of differential aeration or chemical concentration cells and cathodic depolarization.

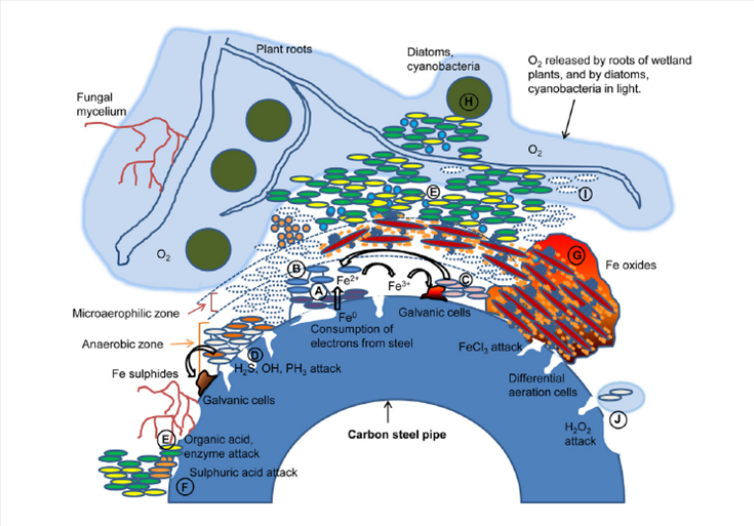


Figure 2.1: Systematic description of MIC mechanisms (Copied from Usher, et al., 2014)

2.1.1 Interactions between MIC and mineral precipitation

Currently, two MIC mechanisms are distinguished to have direct effects on mineral precipitation, they are: galvanic cells and acid attack regarding EMIC and CMIC respectively.

2.1.1.1 Effects of galvanic cells on mineral precipitation

Microorganisms have the ability to precipitate and adsorb a variety of dissolved metal ions into their cells (McLean et al., 2002), which is favorable for the formation of galvanic cells between the metal surface and the biofilm. The presence of galvanic cells can alter the conductivity of low frequency currents (Konhauser, 2009). This effect is essential for the spatial separation of oxidative (anodic) and reductive (cathodic) reactions due to the fact that a higher conductivity allows the free flow of electrons to be transferred from anodic to cathodic sites (Enning and

Garrelfs, 2014). The interesting story is that different precipitated minerals result in different functions of formed galvanic cells. In terms of iron sulphide precipitation, the formed galvanic cells are actually moving the corrosion potential into negative direction and a higher corrosion rate can be established (Javaherdashiti, 2008). If iron carbonate is precipitated, the galvanic cells can be even protective to further corrosion due to the high resistance of iron carbonate to the free flow of electrons (Chan, 2011). In conclusion, the type and magnitude of precipitated minerals are critical for the onset of MIC.

2.1.1.2 Effects of acid attack on mineral precipitation

With the presence of microorganisms, various byproducts of microbial activities, including organic or inorganic acids, are produced. The presence of acids increases the corrosion rate by changing the local pH via hydrogen permeation (Biezma, 2001). In addition to the corrosive effects of produced acids, the acidity of local environment is also essential for the stability of minerals. With a drop in pH, the solubility of some minerals, for instance iron carbonate, increases remarkably. Organic acids can increase the mineral dissolution rate by 2 to 4 times compared to rain water (Huang et al., 2002). Once the protective barrier, such as iron carbonate, is dissolved by the acid, iron will be re-exposed to corrosive agents and leads to the reestablishment of a high corrosion rate. Therefore, it is reasonable to conclude that the acidity of environment is one of keys to understand the interactions between MIC and mineral precipitation.

2.2 Microbially influenced mineral precipitation

The mineral precipitation induced by microbial activities can be described as a double diffusion mixing mineral precipitation process as shown in Figure 2.2. The occurrence of biocorrosion releases metallic ions from the metal surface and creates a concentration gradient towards the reaction region. Released metallic ions react with anions present, for instance carbonate, and induce a concentration gradient of anions from the distant boundary to the reaction region. The concentration of anions at the distant boundary is continuously recharged by groundwater. Meanwhile, the concentration of metallic ions at the metal surface is maintained by the metal corrosion. The concentration gradients lead to molecular diffusion from both metal surface and distant boundary towards the reaction region, and result in mineral precipitation as well as biomass formation.

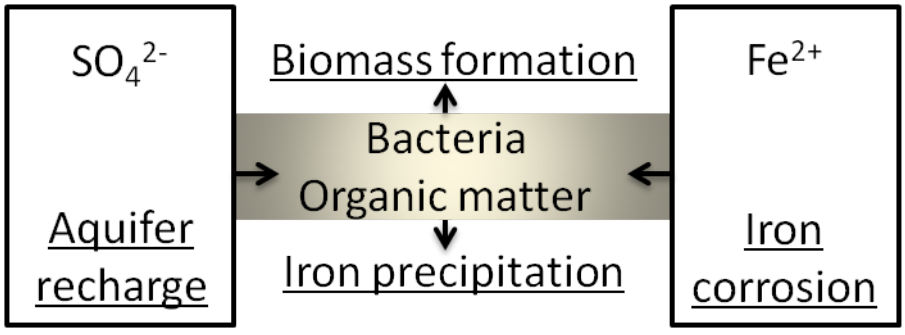


Figure 2.2: Interpretation of microbially influenced mineral precipitation

As Gebrehiwet, et al., (2014) have summarized, the onset of mineral precipitation can be predicted by the degree of local supersaturation as shown in Figure 2.3. Although kinetics of microbial activities are not included in their summary, the position and width of supersaturation zone for a certain mineral is a function of the distance from boundaries and the concentrations of reactants at boundaries. Hence, in this research we aim to demonstrate the effect of distance and boundary concentrations on the position and magnitude of microbially influenced precipitated minerals.

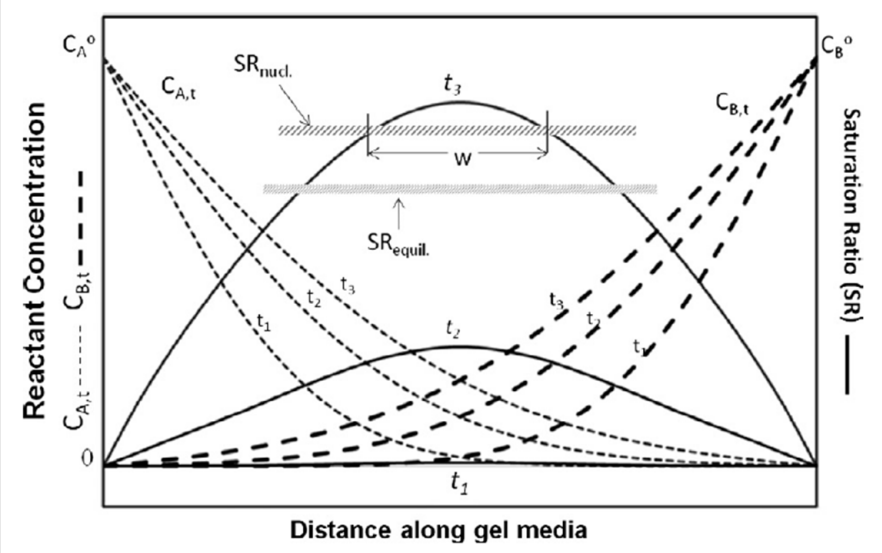


Figure 2.3: Predication of mineral precipitation from local supersaturation degree (Copied from Gebrehiwet, et al., 2014)

2.3 Microbial activities

2.3.1 Microbial growth system

Microbial growth of microorganisms generally can be divided into three processes: catabolism, anabolism and maintenance (Heijnen and Kleerebezem, 1999). Catabolism signifies Gibbs energy generation via a series of redox reactions between electron acceptors and electron donors. Generated Gibbs energy is consumed by anabolism during the formation of biomass. Maintenance is the other energy consumption process, accounting for the endogenous respiration and other demands related to the maintenance of the living microorganisms. A schematic definition of microbial growth is given in Figure 2.4.

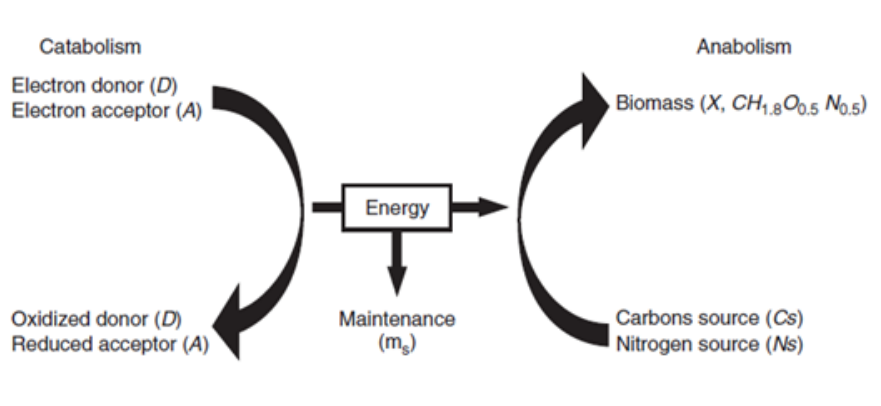


Figure 2.4: Schematic definition of microbial growth (Copied from Heijnen and Kleerebezem, 1999)

The schematic definition of microbial growth clearly emphasizes that Gibbs energy is the key factor governing the growth of microorganism. Gibbs energy is the thermodynamic potential that indicating the system changes from the thermodynamical perspective. In microbial growth system, Gibbs energy on the one hand is the key factor that controlling all microbial activities, on the other hand it is the linking term that helps to couple microbial activities with undergoing biochemical reactions. Hence, a comprehensive investigation of microbially influenced mineral precipitation in the subsurface environment requires an energy-based understanding of microbial activities.

The other key factor in microbial growth is the electron donor and acceptor couple. In nature, different groups of microorganisms have different capacities to catalyze a variety of redox reactions for Gibbs energy production. The electron donor and acceptor can be either organic or inorganic, with a central atom with a variable oxidation state (Hamilton, 2003). When determining redox reactions and corresponding amount of Gibbs energy production, the electron donor and acceptor couples have to be explicitly identified.

2.3.2 Biomass composition

Biomass is the main product of the microbial growth process, the chemical composition of biomass is represented by a simple 1-C formula as: $C_1H_{1.8}O_{0.5}N_{0.2}$ (Heijnen and Kleerebezem, 1999). In practice, the biomass also consists of other elements, for instance S, P, K etc., although their quantities comparing with four major elements are negligible. In terms of mass balance, these minor elements and their contributions are ignored. In this research, the growth of biomass solely depends on carbon source, nitrogen source and electron couples.

2.3.3 Biomass growth kinetics

The formation of biomass is a kinetic process. According to Monod (1949), the formation of biomass consists of several consecutive reversible enzymatic reactions in which the rates and equilibrium constants are interdependent. For the mathematical expression of biomass growth, it is impossible to take the whole interdependent reaction network into consideration. However,

inside the complicated reaction network, we assume the presence of a master reaction which is much slower than all other reactions. Hence, it is sufficient to assume that the master reaction dominates the growth of the biomass formation.

The selection of the master reaction is discussed in Section 2.3.4. With the selected master reaction, a relatively simple empirical relation can be formulated to express kinetic biomass formation. The rate of the master reaction is not constant over time. When the concentrations of all relevant substrates are high, the reaction rate of the master reaction reaches its maximum level. With depletion of one or more substrates, the actual reaction rate may decrease accordingly (O'Toole et al., 2000; Hunt et al., 2004). A hyperbolic equation is introduced to represent this factor in the growth model of biomass (Schäfer et al., 1998; Reichel et al., 2007). The biomass growth is also subjected to endogenous death (Wang and Papenguth, 2007), and this decay process can be expressed by a first order rate relation. Dead biomass is recycled to the carbon pool and reused by other bacteria (Islam and Singhal, 2002). In order to maintain the mass balance, in this research dead biomass is assumed to be reversed to carbon source. The mathematical expression for the biomass growth is shown in Equation 2.1.

$$\frac{\partial C_X}{\partial t} = \mu_{max} \cdot C_X \cdot \frac{C_s}{K_s + C_s} - k_{dec} \cdot C_X \tag{2.1}$$

where C_X is the biomass concentration; K_s is the affinity constant for electron acceptor; μ^{max} is the maximum growth rate; k_{dec} is the first order decay rate and C_s is the limiting substrate concentration.

In case of parallel running biomass formation reactions, the reduction of reaction rate as a result of competitions between microbial processes must be embedded into the Monod-type kinetic equation (Fennell and Gossett, 1998). The inhibition function is discussed in details in Paragraph 2.4.1.1.

2.3.4 Energy-based maximum growth rate estimation

Numerical implementation of the microbial growth process allowing for various growth patterns, quantitative description of substrate conversion and changes in biomass requires a large number of parameters. The amount of parameters increases with increasing diversity of microorganisms in the system. With respect to the generality of the model as well as to reduce the uncertainty of parameters collection, we use the energy-based method developed by Heijnen and Kleerebezem (1999) for estimating maximum growth rate. This energy-based method allows a first approximation of those unknown parameters, and the derivation of the stoichiometric relations regarding diverse redox pathways.

The adopted energy-based method is based on the identification of the Gibbs energy supplying redox reactions and the carbon and nitrogen sources for the microbial growth. It is a step-wise method. An example is given in Appendix A for the derivation of the stoichiometic relation for the microbial growth of sulfate reducing bacteria. This example assumes that acetate

is the carbon source while the nitrogen source is ammonium. The ambient temperature is set as 298.15 K and kept constant.

As stated in Subsection 2.3.3, in order to estimate the growth rate, a master reaction must be determined. Heijnen and Kleerebezem (1999) assume that the rate of catabolic Gibbs energy generation for microbial growth is limited by a maximum rate of electron transfer in the catabolic energy production. Therefore, the energy-based maximum growth rate can be estimated with:

$$q_e^{max} = -3 \cdot exp\{\frac{-69 \cdot 10^3}{R} \cdot (\frac{1}{T} - \frac{1}{298})\} \tag{2.2}$$

$$m_G = -4.5 \cdot exp\{\frac{-69 \cdot 10^3}{R} \cdot (\frac{1}{T} - \frac{1}{298})\} \tag{2.3}$$

$$\mu^{max} = \frac{q_e^{max} \cdot \frac{-\triangle G_{cat}}{\gamma_{D^*}} - m_G}{\triangle G_{Overall}^{min}} \tag{2.4}$$

$$\mu^{max} = \frac{-3 \cdot \frac{-\triangle G_{cat}}{\gamma_{D^*}} - 4.5}{\triangle G_{Overall}^{min}} \cdot exp\{\frac{-69 \cdot 10^3}{R} \cdot (\frac{1}{T} - \frac{1}{298})\} \tag{2.5}$$

where q_e^{max} is the maximum biomass specific electron-transfer rate in the microbial electron transport chain; m_G is the Gibbs energy production rate for maintenance purpose; R is the gas constant and T is the temperature; γ_D^* is the number of electrons transferred in catabolism and it equals to $NoC_D \cdot \gamma_D$ for organic electron donor; NoC_D denotes the carbon length of electron donor; γ_D is the degree of reduction of the electron donor; $\triangle G_{Overall}^{min}$ is the minimum Gibbs energy of dissipation value for the formation of biomass; $\triangle G_{cat}$ is the Gibbs energy changes of this catabolic reaction and μ^{max} is the maximum growth rate. For the example presented in Appendix A, the estimated maximum growth rate is 1.24 day^{-1}.

To define the microbial growth process precisely, other parameters, such as the affinity constant for limiting substrate (K_s), are also required. Unfortunately, no methods are currently available for the estimation of these affinity constants and they have to be assumed or measured separately or obtained by data fitting.

2.3.5 Dominating bacteria in MIC

The inclusion of diverse microorganisms significantly increases the complexities of the system. In order to strike a balance between the generality of the model and the numerical efficiency of the simulation, the microorganism communities included should be evaluated carefully. According to the goals of this research, the selected bacteria should either greatly affect the type or rate of mineral precipitation or alter the kinetics of the system significantly. Besides, the selected bacteria have to be commonly found in the subsurface environment. This research mainly focuses on two types of bacteria: sulfate reducing bacteria and methanogens. The rationale behinds this selection is that both of them are found to have the ability to directly extract electrons

from iron (Mori et al., 2010; Enning et al., 2012) which makes them dominant microorganisms in MIC (Cord-Ruwisch, 2000; Bose et al., 2014). In addition, they play a role in the formation of siderite and iron sulfides (Kuang et al., 2007; Belay and Daniels, 1990).

2.3.5.1 Sulfate reducing bacteria

SRB is bacteria who uses sulfate as electron acceptor. The corresponding reduction process is given in Equation 2.6. For Gibbs energy generation, sulfate can be coupled with various electron donors including organic compounds and solid iron.

$$SO_4^{2-} + 9H^+ + 8e^- \rightarrow HS^- + 4H_2O \tag{2.6}$$

A number of iron sulphides are produced as the products of the iron corrosion influenced by SRB, including mackinawite, greigite, pyrrhotite, marcasite and pyrite (Enning and Garrelfs, 2014). The effects of these precipitated minerals in MIC are controversial. Pyrrhotite (FeS) is considered protective which is able to inhibit the diffusion of ferrous iron from the metallic surface to the aqueous environment (Hansson et al., 2006). However, the protective effect of pyrrhotite film is questioned by Bourdoiseau et al., (2011), who argued that the stability of such a film is low with the continuous presence of SRB. Under these circumstances, the FeS film will be quickly transformed into pyrite (FeS_2) which is a porous film and results in a high corrosion rate (Kato et al., 2012).

2.3.5.2 Methanogens

The methanogens are microorganisms that produce methane from their metabolism. Similar to SRB, the electron source for the formation of methane can be both organic compounds and solid iron. The electron acceptor in methane formation is CO_2 or another carbon source such as acetate. Equation 2.7 shows the reduction reaction for the formation of methane from CO_2.

$$CO_2 + 4H_2 + 8e^- \rightarrow CH_4 + 2H_2O \tag{2.7}$$

Unlike SRB, the mineral precipitated during methane formation process is relatively monotonic (Belay and Daniels, 1990). The precipitated mineral mainly consists of siderite ($FeCO_3$). As discussed in Paragraph 2.1.1.1, the formation of siderite can effectively prevent the free electron flow and subsequently inhibit the corrosion of iron. However, as it for all metal carbonates, siderite is very sensitive to the pH drop. Under low pH conditions, siderite will dissolve (Huang et al., 2002).

2.3.5.3 Competition among bacteria

The interactions among various microorganisms can alter the local environment and subsequently affect the metabolism (Pitonzo et al., 2004; Usher et al., 2014). In a mixed culture, the amount of carbon source and electron donors might be limited. Under these circumstances, microorganisms have to compete for the substrates. From the redox reaction point of view, the

competition of microorganisms can be interpreted as sequential utilization of electrons. This sequential utilization of electrons is important for the dominance of a certain group of microorganism and its corresponding precipitated minerals. Detailed investigation related to the sequential utilization of electrons is presented in Paragraph 2.4.1.1.

2.4 Chemical reactions

2.4.1 Redox reaction

Redox reactions involve electron transfer from one atom to another. The element that looses electrons is called reductant or electron donor, at the same time the oxidant or electron acceptor accepts electrons. In the subsurface environment, the reaction rates of redox reactions are normally low. In this Subsection we focuses on the sequential utilization of electrons and electron donor degradation.

2.4.1.1 Sequential utilization of electrons

Redox zonation has been widely reported in literature (Lovley, D.R. et al., 1988; Islam and Singhal, 2002; Appelo and Postma, 2005). In an anaerobic environment, nitrate is the first one to be reduced and followed by sulfate, eventually methane is formed. This phenomenon can be explained as the weaker-oxidizing electron acceptors are inhibited by the stronger-oxidizing electron acceptors present in the soil solution (Hunter et al., 1998). The pe concept is used to address the strength of those reductants and oxidants. In analogy to pH, pe is defined by Equation 2.8. A high positive value of pe indicates oxidizing conditions and a low negative value represents reducing conditions (Appelo and Postma, 2005). The sequence of predominant redox half reactions can be predicted from the redox diagrams as shown in Figure 2.5.

$$\text{pe}=-\log[e^-] \tag{2.8}$$

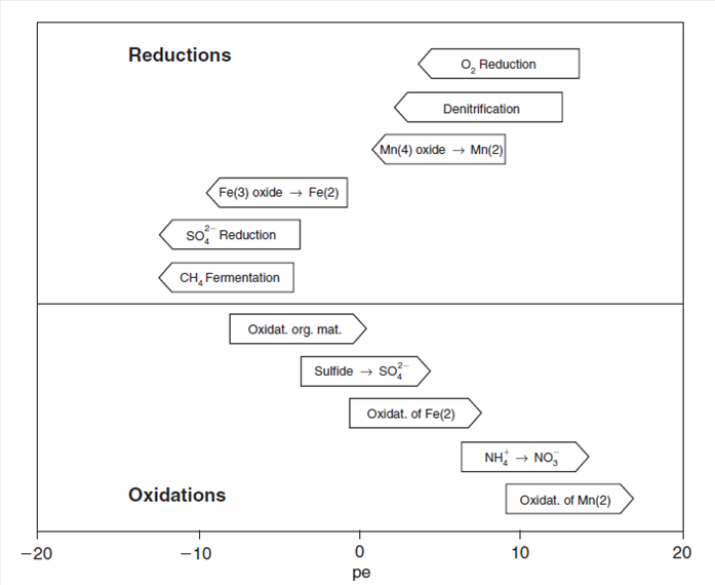


Figure 2.5: Sequence of important redox processes at pH = 7 in natural system (Copied from Appelo and Postma, 2005; Stumm and Morgan, 1996)

Many researchers adopted the method developed by Van Cappellen and Wang (1996) to address the sequential utilization of electrons. This method has a characteristic feature that the total rate of organic carbon degradation is determined independently from the concentration of substances other than organic carbon. Since the total rate of organic carbon degradation, R_C, is well-known, it can be broken down into the contributions of each individual metabolic pathway represented as various reduction reactions. The fraction f_i is defined by:

$$f_i = \frac{R_{e,i}}{R_C} \tag{2.9}$$

$$R_C = \sum_{i=1}^{n} R_{e,i} \tag{2.10}$$

where $R_{e,i}$ is the rate of carbon oxidation by the ith pathway.

In this research the biomass formation reaction is defined as an overall reaction including anabolism and catabolism. The organic matter participates in both processes. In catabolism, it plays the role of electron donor while in anabolism it is the carbon source. For simplicity, an assumption is made here: the calculated fraction f_i which actually expresses the fraction of electron donor consumed by ith catabolism in the half reduction scheme, is identical to the fraction of biomass formed from ith pathway in the overall reaction scheme. This assumption is sufficient since the amount of organic matter consumed by anabolism is negligible comparing with catabolism. Take the SRB biomass formation using acetate (organic matter) as an example. As shown in Equation A.6, the ratio of acetate consumed in anabolism to catabolism is 0.525/9.679, which implies only 5.4% percentage of acetate is used in anabolism as carbon source while the rest (94.5%) is used as electron donor in catabolism.

The fraction f_i calculation is based upon the method developed by Van Cappellen and Wang (1996), who assumed the presence of limiting concentration, $[\mathrm{EA}_i]_{lim}$, for each electron acceptor. When the concentration exceeds this limiting value, the rate relation for that pathway is independent of $[\mathrm{EA}_i]$. However, if the concentration is lower than $[\mathrm{EA}_i]_{lim}$, the rate relation is subjected to a first-order dependency on $[\mathrm{EA}_i]$. For $i = 1 : n-1$, the rate relations can be expressed mathematically as shown below:

If $[\mathrm{EA}_i] > [\mathrm{EA}_i]_{lim}$:

$$f_i = 1 - \sum_{n=o}^{i-1} f_n \tag{2.11}$$

Else:

$$f_i = \left(1 - \sum_{n=o}^{i-1} f_n\right) \frac{[\mathrm{EA}_i]}{[\mathrm{EA}_i]_{lim}} \tag{2.12}$$

For $i = n$

$$f_n = 1 - \sum_{n=o}^{n-1} f_n \tag{2.13}$$

where $f_o = 1$. The sequence of electron acceptors is defined by their oxidation strength, the stronger-oxidizing the electron acceptor, the smaller index it has. For example, in a system that has electron acceptors O_2, NO_3^-, SO_4^{2-} and methanogensis, O_2 is the strongest oxidant, thus f_1 denotes the fraction of electrons used by O_2 and $f_{2,3,4}$ correspond to NO_3^-, SO_4^{2-} and methanogensis respectively.

Notably, the current derivation of the stiochoimetric relation for the biomass formation is implemented with respect to thermodynamics. This implies if one pathway is more energy-favorable, its estimated growth rate of bacteria is higher. In a mixed culture, the most energy-favorable pathway eventually dominates the overall growth pattern. This means that the competition among microorganisms is implicitly included in the estimation of growth rates. Nevertheless, this type of competition is not sufficient to capture the overall competition among microorganisms. In fact, the presence of some microorganisms can totally exclude the growth of other groups. This requires another type of competition to address the interactions among bacteria. This type of competition is called inhibition. Therefore, it is not a duplication to include inhibition relations, the energy-based derivation of growth rate is for the energy affinities while the inhibition is to show the interactions among various pathways.

2.4.1.2 Degradation of organic electron donors

Microbial activities are a function of the available energy. The energy produced from different electron donor/acceptor couples or carbon sources shows significant differences. In the subsurface environment, organic matter is broken down by various processes leading to diverse

byproducts and end-products. An overview of these processes is given in Figure 2.6 (Appelo and Postma, 2005). It should be straightforward to realize that despite of the sequential electron utilization process, the diversity of electron donor and its degradation process also greatly affect the availability of reductants and subsequently alter the growth patterns of bacteria.

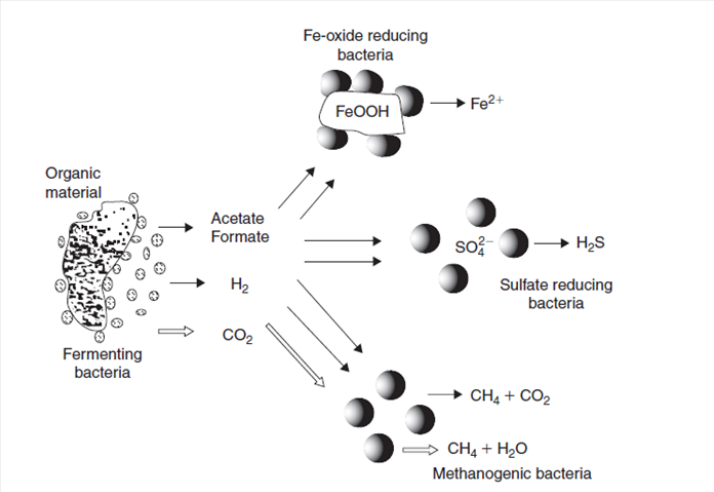


Figure 2.6: Schematic pathway of organic matter decomposition under anaerobic conditions (Copied from Appelo and Postma, 2005)

The abundance of electron donors in the system requires further consideration about the redox pathway. For example, Figure 2.6 clearly states that for SRB, the same electron acceptor can be coupled with acetate, formate, hydrogen and carbon dioxide. For each electron donor/acceptor couple, the resultant overall biomass formation reactions are different. Thus, a question is asked here: do these reactions co-exist? or does one of these reactions dominate its redox pathway? The energy-gain theory might help to answer this question. According to Hoehler (1998), microorganisms utilize the available energy, bringing it down to the minimum threshold which they can achieve. Thus, electron donor/acceptor couple with higher energy gain is rationally assumed to predominate corresponding redox pathway.

From the perspective of numerical efficiency, the implementation of the sequential degradation of organic matters is necessarily simplified. This research applies an energy-based method to estimate the maximum growth rate. In this method, for the same group of bacteria and the corresponding electron acceptor, the organic matter that yields more energy is associated with a higher estimated maximum growth rate. Therefore, unlike Fennell and Gossett (1998) who applied Michaelis-Menten kinetics to denote the parallel degradation of electron donors and coupled biomass formation with electron donor degradation via yield coefficient, this research assumes that, for a certain electron acceptor, the more energetically favorable degradation pathway inhibits all other possible degradation pathways and dominates the corresponding biomass formation process until that organic matter is depleted, in which the degradation rate of electron donor is determined by biomass formation.

2.4.2 Equilibrium reaction

Equilibrium reactions are those reactions that occur instantly. Normally, in the subsurface environment, equilibrium reactions are mainly speciation reactions. The numerical implementation of equilibrium reactions is subjected to three sets of equations: the law of mass action, the mass balance and the electroneutrality. This Subsection uses an example regarding the speciation of carbonic acid system to demonstrate the principles of the numerical implementation of equilibrium reactions.

In Table 2.1, equilibrium reactions related to the carbonic acid system are given.

Table 2.1: Equilibria in the carbonic acid system with approximate equilibrium constant at 293.15 K (Appelo and Postma, 2005)

Reactions	Equilibrium constant
$H_2O \leftrightarrow H^+ + OH^-$	$K_W = [H^+][OH^-] = 10^{-14.0}$
$CO_{2[g]} + H_2O \leftrightarrow H_2CO_3^*$	$K_H = [H_2CO_3^*]/[P_{CO_2}] = 10^{-1.5}$
$H_2CO_3^* \leftrightarrow H^+ + HCO_3^-$	$K_1 = [H^+][HCO_3^-]/[H_2CO_3^*] = 10^{-6.3}$
$HCO_3^- \leftrightarrow H^+ + CO_3^{2-}$	$K_2 = [H^+][CO_3^{2-}]/[HCO_3^-] = 10^{-10.3}$

$$aA + bB \rightleftharpoons cC + dD \tag{2.14}$$

For a generic equilibrium reaction as Equation 2.14, the equilibrium constant K is formulated as Equation 2.15.

$$K = \frac{[C]^c[D]^d}{[A]^a[B]^b} \tag{2.15}$$

In terms of log-transformation, the law of mass action is:

$$c\log[C] + d\log[D] = a\log[A] + b\log[B] + \log K \tag{2.16}$$

For the carbonic acid system, the law of mass action in log-form is:

$$\log[H_2CO_3^*] = \log[P_{CO_2}] - 1.5 \tag{2.17}$$

$$\log[HCO_3^-] = \log[H_2CO_3^*] + \mathrm{pH} - 6.3 \tag{2.18}$$

$$\log[CO_3^{2-}] = \log[H_2CO_3^*] + 2\mathrm{pH} - 16.6 \tag{2.19}$$

where [] denotes the activity of species.

The mass balance equation of dissolved carbonate species is:

$$TIC = m_{H_2CO_3^*} + m_{HCO_3^-} + m_{CO_3^{2-}} \tag{2.20}$$

where TIC is the total dissolved inorganic carbon; $m_{H_2CO_3^*}$ is the amount of $H_2CO_3^*$; $m_{HCO_3^-}$ is the amount of HCO_3^- and $m_{CO_3^{2-}}$ is the amount of CO_3^{2-}.

The electroneutrality is:

$$\triangle e = [H^+] - [HCO_3^-] - 2[CO_3^{2-}] - [OH^-] \tag{2.21}$$

where $\triangle$e represents the net charge that is not participating in the reactions. Due to the fact that $\triangle$e is an invariant and in this model, it is assumed to be zero.

Therefore, with known TIC and pH, the speciation of the carbonic acid system is processed by solving these three sets of equations. The distribution of dissolved carbonate species as a function of pH is visualized in Figure 2.7.

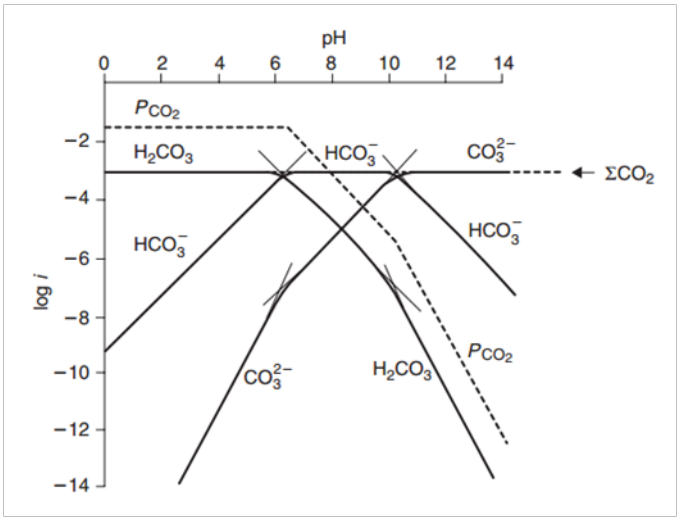


Figure 2.7: The activities of CO_2 species in water at constant total inorganic carbon (Copied from Appelo and Postma, 2005)

2.4.3 Mineral precipitation-dissolution

The general rate law for the changes in solute concentration due to mineral precipitation-dissolution reactions can be written as (Appelo and Postma, 2005):

$$R_m = k_m \frac{A_0}{V} \left(\frac{m_s}{m_0}\right)^b g(C) \tag{2.22}$$

where R_m is the overall reaction rate; k_m is the specific rate; A_0 is the initial surface area of the solid; V is the volume of solution; m_s is the initial moles of solid; m_0 is the moles of solid at a given time and $g(C)$ is a function that comprises the effects of the solution composition on the rate, like pH, the distance from equilibrium and the effects of inhibition.

In the implementation of mineral precipitation rate relation, most of recent work (Hunter et al., 1998; Islam and Singhal 2002) used a first order rate relation to describe the mineral precipitation-dissolution reaction with respect to the mineral saturation state, Ω.

The saturation state is a ratio between IAP (ion activity product) and K_M (solubility product) as:

$$\Omega = \frac{IAP}{K_M} \tag{2.23}$$

The ion activity product shows the activity of the solute and the solubility product is the activity at equilibrium. Thus, when $\Omega = 1$, there is a equilibria between precipitation and dissolution. $\Omega > 1$ denotes the supersaturation state while $\Omega < 1$ represents subsaturation state.

The inclusion of the saturation state leads to the rate relation as follows:

$$R_{m,i} = \begin{cases} k_1^i \cdot (\Omega_i - 1) & \Omega_i > 1 \\ k_2^i \cdot (\Omega_i - 1) \cdot C_{m,i} & \Omega_i \leq 1 \end{cases} \tag{2.24}$$

where R_i denotes the rate relation for mineral i, in which k_1^i is the precipitation rate and k_2^i is the dissolution rate; Ω_i is the saturation state for that mineral and C_i is the amount of solid mineral i.

These rate relations discussed above are not yet comprehensive enough for describing microbially influenced mineral precipitation due to the fact that the stability of iron minerals under redox conditions is a major issue, especially in the presence of microorganisms (Huang et al., 2002; Sun et al., 2008). This stability factor can be included in the function $g(C)$. Take the siderite precipitation as an example. The siderite formation is expressed as Equation 2.25.

$$Fe^{2+} + CO_3^{2-} \rightarrow FeCO_3 \tag{2.25}$$

For a given amount of total inorganic carbon (TIC), the stability of siderite is a function of pH as shown in Equation 2.26 (Appelo and Postma, 2005).

$$TIC = \frac{10^{-10.45}}{[Fe^{2+}]}\left[\frac{[H^+]^2}{10^{-16.6}} + \frac{[H^+]}{10^{-10.3}} + 1\right] \tag{2.26}$$

Accordingly, the stability field of siderite for a given amount of *TIC* can be visualized in Figure 2.8.

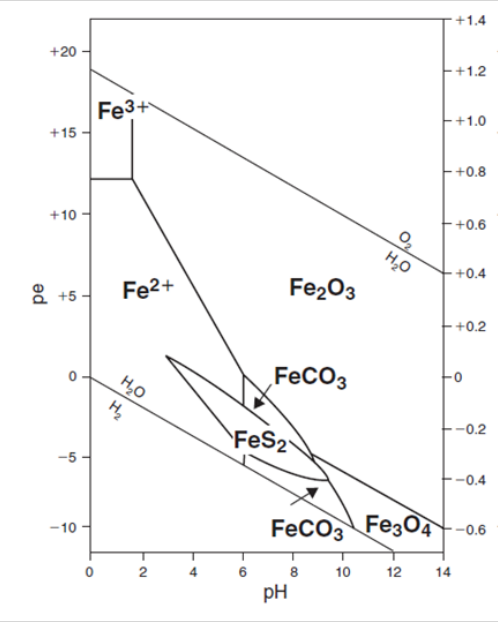


Figure 2.8: Stability of iron minerals at 293.15 K. $TIC = 10^{-2.5}$. (Copied from Appelo and Postma, 2005)

The same law applies to iron sulfide and pyrite, however the stability of these minerals are found to be more related to pS^{2-} $(-\log\left[S^{2-}\right])$ instead of pH (Appelo and Postma, 2005). Theoretically, the inclusion of the stability functions can lead to a more realistic microbially influenced mineral precipitation simulation. However, in the specaition reactions, the pH dependencies are already accounted. In case of siderite precipitation, with pH drops, $\left[CO_3^{2-}\right]$ decreases accordingly as shown in Figure 2.7. Based on current rate relations, it leads to the saturation state moving towards dissolution process, which actually partially expresses the stability of siderite as a function of pH. Therefore, in order not to overestimate the role of pH in mineral precipitation, we decided not to include direct stability functions of minerals in our approach.

2.4.4 Electrical neutrality

In order to enforce the electrical neutrality of the system, balancing species must be introduced. The balancing species must have the following features: no extra dominant reactions will be introduced and the system has to be balanced explicitly. In this research, sodium (Na^+) and chloride (Cl^-) are considered as the balancing species.

The inclusion of balancing species is important for the mineral precipitation simulation since in this model the mineral precipitation rate relations are calculated from the activities of species. With the presence of balancing species, the ionic strength of the solute increases remarkably. As a consequence, the calculated mineral precipitation rate is higher and also more realistic. The activities coefficient of species, Υ_i, are calculated via Davies equation (Appelo and Postma, 2005):

$$\log \Upsilon_i = -Az_i^2 \left(\frac{\sqrt{I}}{1+\sqrt{I}} - 0.3I \right) \tag{2.27}$$

where I is the ionic strength; A is temperature dependent constant, at 298.15 K, $A = 0.5085$ and z_i is charge number of ion i.

The ionic strength is calculated using the Debye-Hückel theory (Appelo and Postma, 2005) as Equation 2.28:

$$I = \frac{1}{2} \sum m_i \cdot z_i^2 \tag{2.28}$$

where m_i is the molarity of ion i.

2.5 Diffusion of reactants

2.5.1 Porous medium properties changes

The definition of porous medium is that a material consisting of a solid matrix with pores in between. In addition, these pores are interconnected and large enough to contain fluid particles, and small enough in order to maintain an interfacial force which controls the shape and location of the interfaces between various fluids (Corey, 1994). The description of porous media mainly requires two terms: porosity, Φ, and intrinsic permeability, k. Porosity denotes the ratio of interconnected pore volume to the total volume of the porous medium. The intrinsic permeability describes the ease with which fluid flows through the porous medium.

In this research, the phase volume changes and its effects on porosity and permeability are included. The precipitated minerals and formed biomass are treated as solid mass. The mathematical expressions of the effects of solid mass accumulation on the properties of porous medium are presented below.

2.5.1.1 Effects of solid mass accumulation on Φ

The biomass-affected porosity is formulated via a macroscopic model developed by Clement et al., (1996b). In their model, the changes in porous media properties are assumed to be caused by the accumulation of solid-phase biomass. They presented a relatively simple formula for the estimation of the fraction of volume occupied by the solid-phase biomass as shown in Equation 2.29.

$$\Phi_s = \frac{X^s \rho_b}{\rho_s} \tag{2.29}$$

$$\Phi_b = \Phi_o - \Phi_s \tag{2.30}$$

where X^s is the mass of microbial cells per unit mass of aquifer solids; Φ_b is the biomass-affected porosity; Φ_s is the volume fraction of the soil-attached porosity; Φ_o is the initial soil porosity; ρ_b is the bulk density of soil and ρ_s is the density of solid phase biomass.

The precipitated mineral affected porosity is treated with the similar concept. According to the modeling work conducted by Islam and Singhal, (2002), the precipitated mineral can be converted into the volume fraction and added to the volume fraction of solid phase biomass to calculate the final changes in porosity. The volume fraction of precipitated mineral is defined by dividing the mass of precipitated mineral per unit volume of aquifer solids by the density of corresponding mineral.

2.5.1.2 Effects of solid mass accumulation on k_{ra}

As stated by Verma and Pruess (1998), the relationship between relative permeability and porosity is a complex issue. It is because this relationship deeply depends on many geometric factors including pore shapes, pore size distribution and conductivity. This research is a REV (representative elementary volume) scale modeling which is a method of volume averaging. This implies no geometric factors associated with the pores are included. Therefore, this research adopts an empirical approach proposed by Clement et al., (1996b) to denote the correlation between porosity and permeability.

$$\frac{k_b}{k_o} = (1 - \frac{\Phi_s}{\Phi_o})^{19/6} \tag{2.31}$$

where k_b is the solid mass-affected permeability and k_o is the initial soil permeability.

2.5.2 Diffusion of aqueous species

The focal point of this research is not the transport process itself. In order to avoid unnecessary complexities and ambiguities, the transport process and the properties of porous medium are simplified. The porous medium is assumed to be fully saturated where the effects of interfacial tension and capillary pressure are excluded. However, in terms of diffusion in porous medium, it is important to take tortuosity into account (Steefel, 2008). Tortuosity is defined as the ratio of the path length that the solute would follow in water alone relative to the path length it would follow in porous medium (Bear, 1972). The effect of tortuosity on molecular diffusion is included via an empirical approach (Steefel, 2008), in which the formation factor, F, is introduced to express the correlation between porosity and tortuosity, as shown in Equation 2.32.

$$F = \frac{1}{\Phi T_L} \tag{2.32}$$

In which case, the diffusive flux becomes:

$$q_{D,i} = -\frac{\Phi}{F} D_i \nabla C_i \tag{2.33}$$

where T_L is tortuosity; $q_{D,i}$ is the diffusive flux of species i and D_i is the dispersion tensor of species i.

The formation factor is commonly determined by Archie's Law as below:

$$F = \frac{1}{a\Phi^m} \tag{2.34}$$

where a is a fitted empirical constant and m is the cementation exponent. we assume their values are 0.71 and 2 respectively (Oelkers, 1996).

Hence, the physical transport equation of dissolved bio-chemical species with the inclusion of the effects of tortuosity is formulated as Equation 2.35. For each aqueous component, the following mass continuity equation describes the coupling between transport process and bio-chemical process:

$$\frac{\partial}{\partial t}(\Phi \cdot C_i) = \nabla \cdot (\frac{\Phi}{F} \cdot D_i \cdot \nabla C_i) + S_i \tag{2.35}$$

where S_i is the bio-chemical sink term.

3 Model development

This Section focuses on the construction of the 1D reactive transport model. This Section clarifies the model assumptions and evaluates some reactive transport models and describes the model structure as well as the coupling algorithm.

3.1 Model assumptions

Some assumptions are made in order to avoid unnecessary complexities and improve the numerical simulation efficiency, they are:

- Temperature is 293.15 K and it is assumed to be constant;
- All processes, states and rates are integrated over the REV;
- All species in all phases are assumed to be homogenous and perfectly mixed;
- All microbial communities are active and the formation of biomass is assumed to occur in the solid phase. The dynamics of biofilm are ignored;
- The porous transport medium is assumed to be fully-saturated and the transport process is not rate-limiting;
- In case of the inclusion of gas formation, the gas volume is set as constant and the gaseous phase is subjected to a predetermined constant pressure. Inert gas, nitrogen, is introduced to balance the pressure;
- There is no solid phase migration.

3.2 Existing reactive transport model evaluation

According to a review by Paraska et al., (2014), reactive transport models have been developed to examine a range of systems and processes including marine organic matter degradation, carbon cycles and groundwater and heavy metal transport. Numerical simulations of flow in porous medium are normally associated with three different length scales: microscopic (pore) scale, macroscopic (REV) scale and field scale (Zhang et al., 2000). Governing equations and dominant processes vary regarding scales. REV (representative elementary volume) scale models are formulated by the method of volume averaging, in which macroscopic variables are assumed to be constant within the magnitude of an averaging volume (Qin and Hassanizadeh, 2014). These macroscopic variables are consistent with laboratory observations and macroscopic scale can be extended to the field scale via up-scaling (Zhang et al., 2000). These characteristics of macroscopic models are favorable for the practical applications. However, the macroscopic variables heavily rely on an accurate description of flow at microscopic (pore) scale in which processes undergoing in pores are directly described. Pore-scale models are closely depended on the pore network generation which is outside the scope of this research. This model is a macroscopic (REV) scale model.

This research briefly evaluates several REV scale reactive transport models regarding microbially influenced mineral precipitation process. Walter et al., (1994) coupled PLUME2D (transport module) to MINTEQA2 (equilibrium geochemistry module) to simulate the transport of multiple reactive substances in the subsurface environment. This work adopts local equilibrium assumption in which the effects of reactions time-scale are ignored. This solution gains a higher efficiency and a relatively comprehensive reaction network regarding speciation reactions while all dominant reaction kinetics are filtered out. Reichel et al., (2007) develop a matrix-based solution to investigate the chemical and biological processes in the subsurface environment. The matrix-based solution is easily accessible for various bio-related reactions and any specific kinetics. Therefore, it enables a detailed investigation of the complexities of mixed-culture microorganism communities. The limitation of this model is obvious: equilibrium reactions and mineral precipitation reactions are not included. Hunter et al., (1998) take a step further. They develop their model, BIORXNTRN, with great emphasis on the comprehensive representation of full set of reactions, in which the time-scale effects of reactions are explicitly defined and the kinetics of reactions are well implemented. However, this model is subjected to an essential limitation: the correlations between the reactions and the phase-volume changes are ignored. In addition to the constructions of reaction network, other researchers (Islam and Singhal, 2002; Schäfer et al., 1997) include phase exchanges in their models. In the model, LTM1D, developed by Islam and Singhal (2002), the bio-chemical reactions are interconnected with solid-phase volume changes via a macroscopic approach.

In conclusion, the comprehensive representation of reaction network should take the time-scale effects into account, and effects of biochemical reactions should be integrated into the properties changes of porous medium. This model applies the ORCHESTRA class interface developed by van Turnhout et al., (2015) in which ORCHESTRA is an equilibrium reaction processor to establish a comprehensive representation of reaction network. Effects of biochemical reactions on the properties changes of porous medium are addressed by macroscopic and empirical approaches.

3.3 Model structure

3.3.1 Model components

This model consists of three components: EXCEL and MATLAB are software environments, ORCHESTRA is a chemical equilibrium module which is implemented as a Java class. EXCEL is used to create a scenario. In MATLAB, a tool box consisting of scripts, functions and classes is created and it enables: 1) solve the kinetic and equilibrium reactions and diffusion process using the built-in solver (*ode*) and the ORCHESTRA class interface; 2) process and visualize the simulation results.

3.3.2 Coupling algorithm

The governing equation is:

$$\frac{\partial}{\partial t}C_{ref}^{\bar{T}} = -\nabla \cdot q_D + R(\bar{C^D}) \tag{3.1}$$

$$q_{D,i+1/2} = -(\frac{\Phi}{F}D)_{i+1/2}\frac{\partial C_{ref,i}^{\bar{T}}}{\partial x_i} \tag{3.2}$$

where $C_{ref}^{\bar{T}}$ denotes the vector of total concentrations in reference state and $\bar{C^D}$ denotes the vector of derived concentrations. The distinction of C_{ref}^{T} and C^D is given in Paragraph 3.3.3.1.

The method of lines is used to replace the spatial derivative with an algebraic approximation as shown in Equation 3.3 and 3.4. The transport domain is discretized into nodes (i) and internodes ($i+1/2$).

$$\frac{\partial C_{ref,i}^{\bar{T}}}{\partial x_i} = \frac{C_{ref,i}^{\bar{T}} - \bar{C_{ref,i-1}^{T}}}{x_i - x_{i-1}} \tag{3.3}$$

$$\frac{\partial q_{D,i+1/2}}{\partial x_{i+1/2}} = \frac{q_{D,i+1/2} - q_{D,i-1/2}}{x_{i+1/2} - x_{i-1/2}} \tag{3.4}$$

Therefore, the governing equation is rewritten as:

$$\bar{C_{ref}^{T,t+1}} - C_{ref}^{\bar{T},t} = \left[-\nabla \cdot q_D(C_{ref}^{\bar{T},t}) + R(\bar{C^D})\right] \cdot \triangle t = \mathrm{NF} \cdot \triangle t \tag{3.5}$$

where NF is the netto flux which calculates the total rate of $C_{ref}^{\bar{T}}$ changes as a function of $C_{ref}^{\bar{T}}$ and $\bar{C^D}$.

NF is passed to the *ode* solver which integrates the interested processes over time. The *ode* solvers use self-adaptive timestep to optimize the time integral. The algorithm used to calculate NF is presented below:

Algorithm 1 Fully coupled reactive transport modeling

EXCEL(scenario construction)
⇓
MATLAB
⇒Initialization
⇒*ode* solver

- NF
  - Calculate derived concentrations using ORCHESTRA for each node;
  - Using species concentrations calculate microbial growth kinetics;
  - Using species concentrations calculate mineral precipitation kinetics;
  - Using species concentrations calculate gas-liquid exchange kinetics;
  - Diffusion rates;
  - Add all rates to the total rate.

⇒Results visualization.

3.3.3 Implementation details

3.3.3.1 Selection of reference states

As stated by Yeh and Tripathi (1989), the selection of variables for the formulation of kinetic reactions and transport mass balance is the first important step in developing reactive transport model. This model defines two classes of species, C^T_{ref} and C^D. $C^T_{ref,i}$ represents the total amount of ith substance in the system in reference state. In other word, C^T_{ref} are the parent species for the speciation reactions. C^D are derived concentrations after specaition reactions.

The relation between C^T_{ref} and C^D is shown in Equation 3.6.

$$C^T_{ref,i} = \sum C^D_i \tag{3.6}$$

Ideally, C^T_{ref} should include all those species involved in kinetic reactions. However, this is not always possible. If the reaction network consists of multiple kinetic reactions referring multiple species from the same acid system, it is only possible to define one reference state. Under this circumstance, changes in those species other than the selected reference state induced by kinetic reactions simultaneously alter the H^+/OH^- balance and cause distorted pH calculation.

There are two possible solutions to solve this problem. The first solution is to uniform those stoichiometric relations of all kinetic reactions manually: only use the reference state to express kinetic reactions. This solution is especially favorable when the number of kinetic reactions is limited. However, as the number of kinetic reactions increasing, it is getting more and more difficult to manipulate the stoichiometric relations, sometimes even impossible. The

other solution is to compensate the H^+ distortion by adding/deducting H^+ to/from the system. This solution requires extra consideration in balancing the $H^+/OH^-$of the system, while the original stoichiometric relations can be kept. In case of abundant kinetic reactions, this solution is more efficient.

The aforementioned H^+ denotes the acidity of the solute. For a neutral solute, the concentration of H^+ is 0 and the corresponding pH is 7. For a acid solute, the concentration of H^+ increases above 0. When the concentration of H^+ drops below 0, it indicates an alkaline condition. Hence, negative value of the concentration of H^+ is possible.

3.3.3.2 Single ORI versus multiple ORIs

There are two solutions to initialize the ORCHESTRA calculator (ORI): one is single ORI solution and the other one is multiple ORI solution. Single ORI means only one ORI is initialized and it is used to process the calculation of equilibrium reactions for all cells. In multiple ORI solution, multiple ORIs are initialized and assigned to each cell separately as well as to the calculation of equilibrium reactions.

In the calculation procedure of ORCHESTRA, ORI starts with an initial guess and processes the calculation progressively. At the end of each round of calculation, the ORI records the end value and regards it as the initial guess for the coming calculation. If the single ORI solution is applied, ORI uses $C_i^{nN,t-1}$, the concentration in the last cell from previous timestep, as the initial guess to calculate $C_i^{1,t}$, the concentration in the first cell at current timestep. However, the concentrations of some species over the whole domain might vary significantly. In this case, the difference between $C_i^{nN,t-1}$ and $C_i^{1,t}$ can be large. It causes a lot of time for ORI to converge the initial guess with the real concentration in that cell. Multiple ORI solution is free from this initial guess problem. In multiple ORI solution, each cell has it own ORI. All of these ORIs record $C_i^{1\cdots nN,t-1}$ respectively and use them as the initial guess for next calculation. Although the concentration changes over time, these temporal differences are much smaller comparing with spatial differences, particularly when the timestep is small and the domain size is large. In general multiple ORI solution is more stable and efficient regarding our descretization which is based on the method of lines.

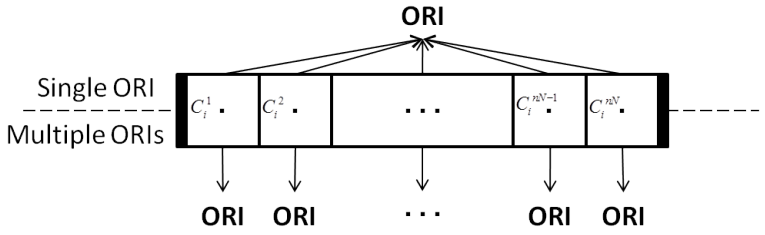


Figure 3.1: Multiple ORI versus single ORI

4 Model testing

4.1 Microbially catalyzed urea hydrolysis

This scenario is proposed with respect to a microbially catalyzed urea hydrolysis experiment conducted by van Paassen. The urea hydrolysis produces reactants that reacting with calcium present, and the microbially controlled kinetics of urea hydrolysis dominate this process. This experiment measured the pH front progression as an indicator of the reaction progresses. In order to simulate the pH front progression, the model should be able to simulate the microbially catalyzed urea hydrolysis kinetics (source of changes), kinetic calcite precipitation (system response), diffusion (spatial spread of changes) and speciation reactions (pH calculation). The simulated pH front progression is compared with experimental observations present.

4.1.1 Experiments description

The set-up of this experiment is shown in Figure 4.1. The yellow part indicates the reaction region which is about 12 cm, on where dissolved chemical compounds are homogeneously distributed with concentrations listed in Table 4.1. The phenol is used as the reaction indicator, when the local pH is below 6.8, the phenol is yellow while the local pH is above 8.2, it shows pink. Initially the background pH is adjusted with HCl and maintained at 3.7. Therefore, the phenol is yellow. As the reaction progresses, the local pH rises and phenol turns to pink. Color change attribute to the advancement of the reaction front. The test tube is sealed with paraffin wax in order to prevent ambient gas from influencing the experiment.

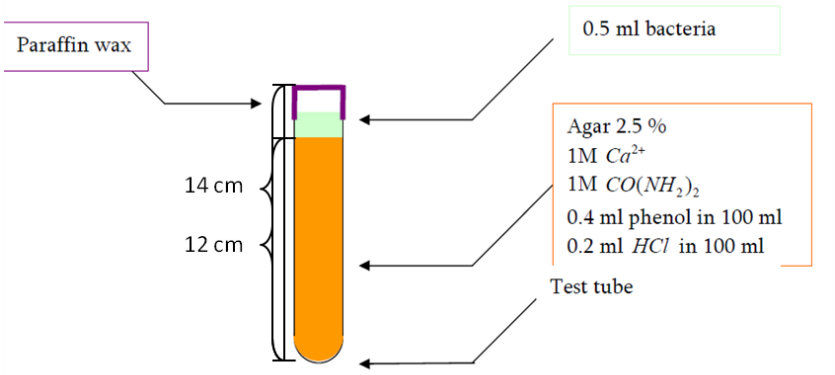


Figure 4.1: Microbially catalyzed urea hydrolysis experimental set-up (Provided by van Paassen)

Table 4.1: Initial conditions in the urea hydrolysis simulation

Initial concentrations

Compounds	Ca^{2+}	urea	Cl^-	H^+
Concentration /mol L^{-1}	1	1	$2+2\times10^{-4}$	2×10^{-4}

Half a ml of bacteria solution with a concentration of 0.5 g L^{-1} is placed on top of the reaction region. Bacteria are assumed to stay in place and catalyze the urea hydrolysis at the upper boundary. Subsequently, byproducts of urea hydrolysis diffuse into the system and cause other reactions. The overall reaction network is presented in Table 4.2, in which the hydrolysis and calcite precipitation are considered as kinetic reactions while all other reactions are assumed to be equilibrium reactions. The rate relation for microbially catalyzed urea hydrolysis is shown in Equation 4.1 and Equation 2.24 is used to depict the calcite precipitation process. In this experimental set-up, the bacteria are regarded as pseudo catalyst, they control the kinetics of urea hydrolysis but are excluded from the reaction network. Therefore, the amount of bacteria is assumed to be constant. This assumption is valid for a short duration of the experiment.

$$R_{urea} = \mu_{max,urea} \cdot \frac{C_{urea}}{K_{s,urea} + C_{urea}} \cdot C_X \tag{4.1}$$

where R_{urea} is urea hydrolysis rate; C_{urea} is the urea concentration; $\mu_{max,urea}$ is the maximum urea hydrolysis rate; $K_{s,urea}$ is the affinity constant for urea and C_X is the bacteria concentration.

Table 4.2: Reaction network in the microbially catalyzed urea hydrolysis experiment

Kinetic reactions	Equilibrium reactions
$\text{urea} + 2H_2O \rightarrow 2NH_4^+ + CO_3^{2-}$	$NH_4^+ \leftrightarrow NH_3 + H^+$
$Ca^{2+} + CO_3^{2-} \rightarrow \text{Calcite}$	$H_2O \leftrightarrow H^+ + OH^-$
	$CO_{2[g]} + H_2O \leftrightarrow H_2CO_3^*$
	$H_2CO_3^* \leftrightarrow H^+ + HCO_3^-$
	$HCO_3^- \leftrightarrow H^+ + CO_3^{2-}$
	$CaHCO_3^+ \leftrightarrow H^+ + Ca^{2+} + CO_3^{2-}$
	$CaOH^+ + H^+ \leftrightarrow Ca^{2+} + H_2O$
	$CaCO_{3[aq]} \leftrightarrow CO_3^{2-} + Ca^{2+}$

4.1.2 Numerical simulation

The reaction tube is considered to be a closed system. The Neumann boundary condition is applied on both boundaries, where the flux outside the reaction region is set to be zero. Because the agar gel is considered to be a non-porous medium here, the mineral precipitation affected porosity and permeability are ignored. The transport process is considered to be dominated by diffusion. The diffusion coefficient in agar gel is extrapolated from literature. The diffusion coefficient in 1.5% agar gel is measured as $(2.5 \pm 0.2) \times 10^{-10}$ m^2 s^{-1} (Støren et al., 2003), which is equivalent to 0.215 ± 0.015 cm^2 d^{-1}. The diffusion coefficient in 5% agar gel is reported as 1.19 cm^2 d^{-1} (Shaw and Schy, 1981). Accordingly the diffusion coefficient for 2.5% agar gel is estimated as 0.5 cm^2 d^{-1} as shown in Figure 4.2. All species are assumed to have the same diffusion coefficient.

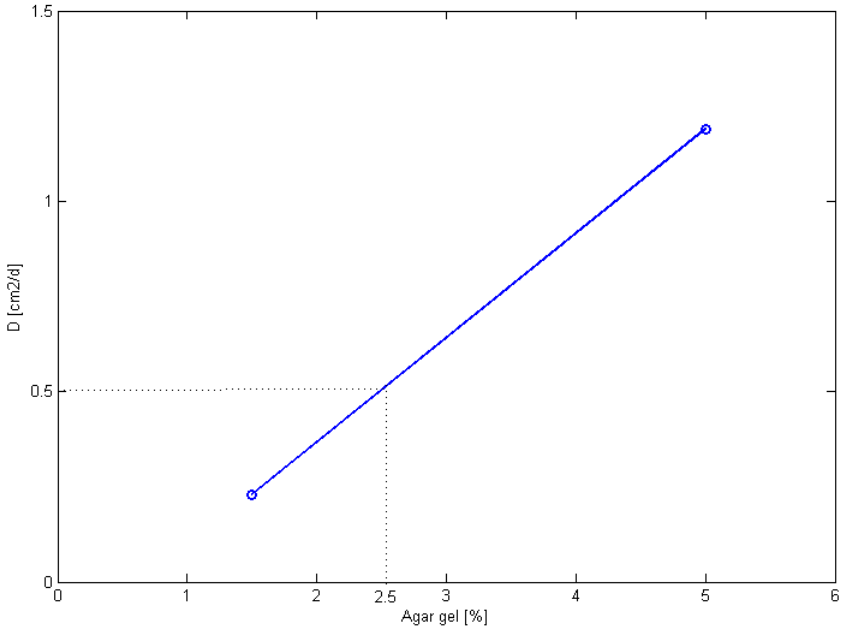


Figure 4.2: Estimated diffusion coefficient for 2.5% agar gel

Based on the minimum data sampling interval, the interval of data sampling in this numerical simulation is set as 0.04 d and the simulation duration is 6 d. The domain is discretized into 100 cells non-uniformly. It is denser at the upper boundary in order to capture the sharp front induced by urea hydrolysis.

Table 4.3: Parameters used in the urea hydrolysis simulation

Parameter	Value	Unit	Description	Source
$K_{M,Calcite}$	3.31×10^{-9}	$mol^2\ L^2$	Solubility product	A
$k_1^{Calcite}$	1.2×10^{-5}	$mol\ d^{-1}\ L^{-1}$	Precipitation rate	B
$k_2^{Calcite}$	1.1×10^{-5}	d^{-1}	Dissolution rate	A
$\mu_{max,urea}$	71.712	$mol\ g^{-1}\ d^{-1}$	Maximum growth rate	C
$K_{s,urea}$	0.1	$mol\ L^{-1}$	Affinity constant	C

A: from Hunter et al., (1998); B: fitted against experimental observations; C: Provided by van Paassen.

Table 4.4: Transport and discretization parameters used in the urea hydrolysis simulation

Transport and discretization parameters	
Length of domain	12 cm
Number of cells	100
Simulation duration	6 d
Sampling interval	0.04 d
Diffusion coefficient	0.5 cm^2 d^{-1}

4.2 Calcite precipitation under double diffusion

The experiments conducted by Gebrehiwet, et al., (2014) used a double diffusion configuration which is conceptually identical to the configuration of microbially influenced mineral precipitation as shown in Figure 4.3. Their research provides real-time experimental observations as well as numerical simulation results. Based upon the availability of detailed experimental observations and numerical simulation results, one carbonate series, called c7uu in Gebrehiwet, et al., (2014), is simulated with our model. The experimental observations present the distribution of calcite and the simulation results help to correlate calcite precipitation to the porosity reduction. In order to predict the calcite distribution, the model should be able to simulate the kinetic calcite precipitation, porosity reduction, diffusion and speciation reactions.

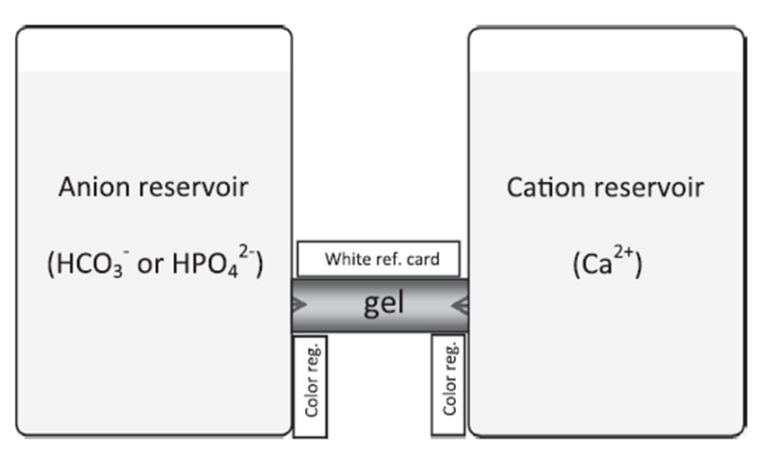


Figure 4.3: Double diffusion configuration of calcium precipitation experiment (Copied from Gebrehiwet, et al., 2014)

The reaction network for c7uu experiment is listed in Table 4.5. The transport medium is a gel with an initial porosity of 0.9 and its diffusion coefficient is selected as 5×10^{-6} cm^2 s^{-1} for all aqueous species. The length of the reaction region is 3.5 cm and the duration of simulation is 47 d. The boundary conditions are given in Table 4.6. The calcite is assumed to be the only precipitated mineral. Due to the fact that our model used different rate relation to depict the kinetics of mineral precipitation, the rate parameters used in our simulation are

determined independently. Discussions regarding the effects of rate parameters are presented in Subsection 5.4. Table 4.7 gives parameters used in this simulation. Table 4.8 shows the transport and discretization parameters. In the double diffusion configuration, the Dirichlet boundary is applied on both boundaries where the concentrations at two boundaries are fixed.

Table 4.5: Reaction network for c7uu experiment (Gebrehiwet, et al., 2014)

Kinetic reactions	Equilibrium reactions
$Ca^{2+} + HCO_3^{2-} \rightarrow$ Calcite+H^+	$H_2CO_3^* \leftrightarrow H^+$+$HCO_3^-$
	$HCO_3^- \leftrightarrow H^+$+$CO_3^{2-}$
	$H_2O \leftrightarrow H^+$+OH^-
	$CaHCO_3^+ \leftrightarrow H^+ + Ca^{2+} + CO_3^{2-}$
	$CaOH^+ + H^+ \leftrightarrow Ca^{2+} + H_2O$
	$CaCO_{3[aq]} \leftrightarrow CO_3^{2-} + Ca^{2+}$

Table 4.6: Boundary conditions used in the calcite precipitation simulation

Boundary conditions		
Reservoir	Anion reservoir	Cation reservoir
Compounds	Ca^{2+}	HCO_3^-
Concentrations	0.1 mol L^{-1}	0.1 mol L^{-1}

Table 4.7: Parameters used in the calcite precipitation simulation

Parameter	Value	Unit	Description	Source
Φ	0.9	-	Porosity	A
k_{ra}	1.0	-	Relative permeability	A
$K_{M,Calcite}$	3.31×10^{-9}	$mol^2\ L^2$	Solubility product	B
$k_1^{Calcite}$	3.3×10^{-6}	mol d^{-1} L^{-1}	Precipitation rate	B
$k_2^{Calcite}$	1.1×10^{-5}	d^{-1}	Dissolution rate	B
$\rho_{Calcite}$	2.71	g cm^{-3}	Density	C
$M_{Calcite}$	100.09	g mol^{-1}	Molar mass	D

A: estimated from gel properties; B: from Hunter et al., (1998); C: from Islam and Singhal, (2002); D: from theory

Table 4.8: Transport and discretization parameters used in this calcium precipitation simulation

Transport and discretization parameters

Length of domian	3.5 cm
Number of cells	50
Simulation duration	47 d
Sampling interval	0.1 d
Diffusion coefficient	0.432 $cm^2 d^{-1}$

4.3 Microbially influenced mineral precipitation

As described in Subsection 2.2, microbially influenced mineral precipitation has been translated into a double diffusion mixing mineral precipitation process. This scenario tests the effects of varying boundary concentrations and distance on this specific mineral precipitation process. This scenario is further subdivided into two subscenarios. Subscenario 1 is to test the effects of varying boundary concentrations, in which three series of ferrous iron boundary concentrations (F1, F2 and F3) and three series of sulfate boundary concentrations (S1, S2 and S3) are proposed. Subscenario 2 is for the demonstration of the effects of distance on the microbially influenced ferrous iron precipitation, and it consists of three series: L1, L2 and L3.

4.3.1 Varying boundary concentrations

In Subsection 2.3.5, we described SRB as one of the most corrosive bacteria in the subsurface environment. For simplicity, this numerical simulation only accounts for SRB. In case of SRB induced corrosion (Venzlaff et al,. 2013), SRB has the ability to severely corrode metallic substrates with a rate up to 0.7 mm $year^{-1}$. King et al., (1973) investigated the effects of ferrous iron concentration in the growth medium of SRB on the corrosion of mild steel. They collected field data which enables the establishment of the correlation between iron corrosion rate and ferrous iron concentration in the medium as shown in Figure 4.4. In most of case, the ferrous iron concentration is found below 100 mmol L^{-1}. At a corrosion rate of 0.44 mm $year^{-1}$, the ferrous iron concentration is significantly higher, which is 510 mmol L^{-1}. For this subscenario, we propose three boundary concentrations for ferrous iron indicating various degrees of MIC. In terms of severe MIC (F3), the boundary ferrous iron concentration is extrapolated to 0.5 mol L^{-1}. The moderate MIC (F2) corresponds to 0.25 mol L^{-1}, and the mild MIC (F1) is equivalent to the boundary concentration of ferrous iron of 0.1 mol L^{-1}.

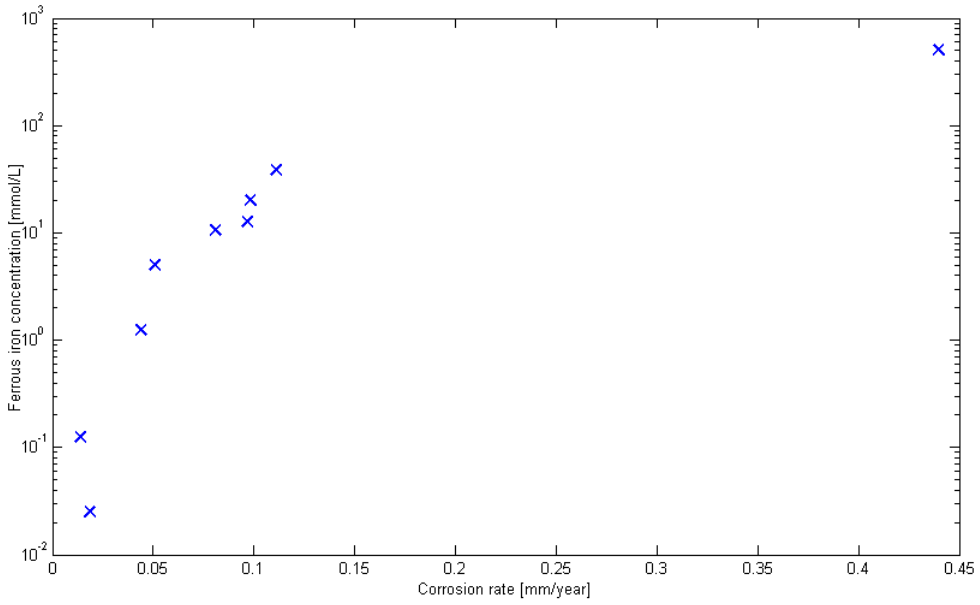


Figure 4.4: Corrosion rate and ferrous iron concentration correlation (King et al., 1973)

In this double diffusion configuration, the other diffusion boundary is considered to be the electron acceptor (sulfate). Regarding various environmental conditions, three series of sulfate boundary concentrations are defined. According to Habicht et al., (2002), the natural concentration of sulfate in freshwater lake sediment is 300 μmol L^{-1}, and in sea water it is 20 mmol L^{-1}. We assume two series (S1 and S2) of boundary sulfate concentrations respectively and in case of engineered conditions, the sulfate concentration can be artificially maintained at high value, for instance 0.2 mol L^{-1}, which we consider to be the third series (S3).

The growth of bacteria also requires carbon source, electron donor and nitrogen source. The carbon source and electron donor are assumed to be lactate, and ammonium is the nitrogen source. The lactate and ammonium concentrations are selected from Schäfer et al., (1998) and Islam and Singhal, (2002) respectively, which are considered to be a condition of abundance. The initial concentration of biomas is assumed to be 0.01 mol L^{-1}(Reichel et al., 2007). Besides, sodium chloride is introduced to keep the electrical neutrality of the solute. Table 4.9 lists the initial concentrations of this simulation. The summary of experimental conditions is presented in Table 4.10.

Table 4.9: Initial concentrations in microbially influenced mineral precipitation simulation

Initial concentrations

Compounds	SO_4^{2-}	Biomass	NH_4^+	Lac^-	Fe^{2+}
Concentration /mol L^{-1}	0	0.01	0.02	0.05	0

Table 4.10: Summary of microbially influenced mineral precipitation numerical experiments

Series	SO_4^{2-} /mol L^{-1}	Fe^{2+} /mol L^{-1}	Description
S1	3×10^{-4}	0.25	Freshwater, moderate corrosion
S2	0.02		Seawater, moderate corrosion
S3	0.2		Engineered condition, moderate corrosion
F1	0.02	0.1	Seawater, mild corrosion
F2		0.25	Seawater, moderate corrosion
F3		0.5	Seawater, severe corrosion

With the presence of microorganisms, the precipitation kinetics are much more complicated. The precipitation of pyrite is an example. As stated in Paragraph 2.3.5.1, the precipitated pyrrhotite will be quickly transformed into pyrite with the continuous presence of SRB. The formation of pyrrhotite from ferrous iron and hydrogen sulfides is well known as Equation 4.2. The transmission of pyrrhotite is formulated as Equation 4.3 accordingly.

$$Fe^{2+} + HS^- \rightarrow FeS + H^+ \tag{4.2}$$

$$7FeS + SO_4^{2-} + 6HS^- + 2H^+ \rightarrow 7FeS_2 + 4H_2O \tag{4.3}$$

Although the transformation step is reported as a fast reaction, it's still subjected to specific kinetics, as shown in Equation 4.3 the formation of pyrite from pyrrhotite is a redox reaction and needs sulfate/sulfide couple to process the electron transfer. Currently, no relevant kinetics of this transformation process have been found. In the absence of supporting experimental observations, it is improper to impose any artificial kinetic relationship. In order to avoid unnecessary complexity and ambiguity, this simulation only takes the pyrrhotite precipitation into account, the transformation step is ignored. In total, two types of minerals are considered in this simulation: siderite and pyrrhotite.

The reaction network for the microbially influenced mineral precipitation in the presence of SRB is shown in Table 4.11. Table 4.12 is for the numerical discretization. The iron corrosion boundary is considered as a closed boundary, where the presence of iron surface prevents the flux. Therefore, the Neumann boundary condition is applied on the iron corrosion boundary. The other sulfate boundary regarding groundwater recharge is an open boundary, where substances have the access to enter the groundwater. We apply the Dirichlet boundary for the sulfate boundary.

Table 4.11: Reaction network of the microbially influenced mineral precipitation in the presence of SRB

Biomass formation	
$3.13Lac^- + 0.2NH_4^+ + 4.171SO_4^{2-} \rightarrow B_x + 8.391HCO_3^- + 4.171HS^- + 0.4H_2O + 1.29H^+$	
$B_x + 0.5H_2O \rightarrow 0.333Lac^- + 0.2NH_4^+$	
Mineral precipitations	Equilibrium reactions
$Fe^{2+} + HCO_3^{2-} \rightarrow$ Siderite+H^+	$NH_4^+ \leftrightarrow NH_3 + H^+$
$Fe^{2+} + HS^- \rightarrow$ Pyrrhotite $+ H^+$	$H_2CO_3^* \leftrightarrow H^+ + HCO_3^-$
	$HCO_3^- \leftrightarrow H^+ + CO_3^{2-}$
	$H_2O \leftrightarrow H^+ + OH^-$
	$HLac \leftrightarrow Lac^- + H^+$
	$NaHCO_3 \leftrightarrow Na^+ + HCO_3^-$
	$NaCO_3^- \leftrightarrow Na^+ + CO_3^{2-}$
	$H_2S \leftrightarrow H^+ + HS^-$
	$HS^- \leftrightarrow H^+ + S^{2-}$
	$HSO_4^- \leftrightarrow H^+ + SO_4^{2-}$
	$H_2SO_4 \leftrightarrow H^+ + HSO_4^-$

Table 4.12: Transport and discretization parameters used in the microbially influenced mineral precipitation simulation

Transport and discretization parameters	
Length of domain	5 cm
Number of cells	60
Simulation duration	30 d
Sampling interval	0.1 d
Diffusion coefficient	1.73 cm^2 d^{-1}

4.3.2 Varying distances

This subscenario consists of three series with various distances. In the L1 the distance is 5 cm, in the L2 the distance is 10 cm and in the L3 the distance is 20 cm. The reaction network, initial concentrations and numerical discretizations are same with the varying boundary concentrations subscenario. The same boundary concentrations as used in the series S2/F2 are applied here. Parameters used in this simulation are listed in Table 4.13.

Table 4.13: Parameters used in the microbially influenced mineral precipitation simulation

Parameter	Value	Unit	Description	Source
Φ	0.4	-	Porosity	A
k_{ra}	1.0	-	Relative permeability	A
$K_{M,Siderite}$	3.89×10^{-11}	$mol^2\ L^2$	Solubility product	F
$K_{M,Pyrrhotite}$	2.51×10^{-14}	$mol^2\ L^2$	Solubility product	F
$k_1^{Siderite}$	6.94×10^{-10}	$mol\ d^{-1}\ L^{-1}$	Precipitation rate	F
$k_2^{Siderite}$	1.16×10^{-9}	d^{-1}	Dissolution rate	F
$k_1^{Pyrrhotite}$	5.79×10^{-10}	$mol\ d^{-1}\ L^{-1}$	Precipitation rate	F
$k_2^{Pyrrhotite}$	5.79×10^{-10}	d^{-1}	Dissolution rate	F
ρ_{Soil}	1.8	$g\ cm^{-3}$	Density	D
$\rho_{Siderite}$	3.9	$g\ cm^{-3}$	Density	D
$\rho_{Pyrrhotite}$	4.7	$g\ cm^{-3}$	Density	D
$\rho_{Biomass}$	0.07	$g\ cm^{-3}$	Density	D
$M_{Siderite}$	115.86	$g\ mol^{-1}$	Molar mass	B
$M_{Pyrrhotite}$	87.91	$g\ mol^{-1}$	Molar mass	B
$M_{Biomass}$	24.6	$g\ mol^{-1}$	Molar mass	B
$\mu_{max,SRB(Lac^-)}$	2.528	d^{-1}	Maximum growth rate	C
k_{dec}	0.016	d^{-1}	Decay rate	D
K_{s,Lac^-}	3.5×10^{-2}	$mol\ L^{-1}$	Affinity constant	E
$K_{s,SO_4^{2-}}$	3.3×10^{-2}	$mol\ L^{-1}$	Affinity constant	D

A: estimated from sandy soil environment; B: from theory; C: calculated from Subsection 2.3.4; D: from Islam and Singhal, (2002); E: estimated from Islam and Singhal, (2002), the affinity constant of acetate is used as the affinity constant of lactate; F: from Hunter et al., (1998).

5 Results and discussions

5.1 Urea hydrolysis simulation

The measured progression of the reaction front data is listed in Table 5.1. Figure 5.1 shows the progression of pH $>$ 8.2 front after 2 days, it clearly shows that there is a color transition zone of the pH front which is approximately 0.6 cm. The presence of the color transition zone affects the accuracy of measured pH front advancement, therefore the error bar is introduced to compensate for the eyeballing errors.

Table 5.1: Measures of the pH limit progression (Provided by van Paassen)

Time /d	Progression of the pH limit /cm
0	0
0.0417	0.3
0.0833	0.7
0.1250	1
0.4167	1.5
0.7500	2
1	2.5
1.1250	2.7
1.4583	3
1.6667	3.5
1.9167	4
2.1042	4.2
2.7292	4.8
3.0625	5
3.6875	5.8
4.1042	6
4.7708	6.3

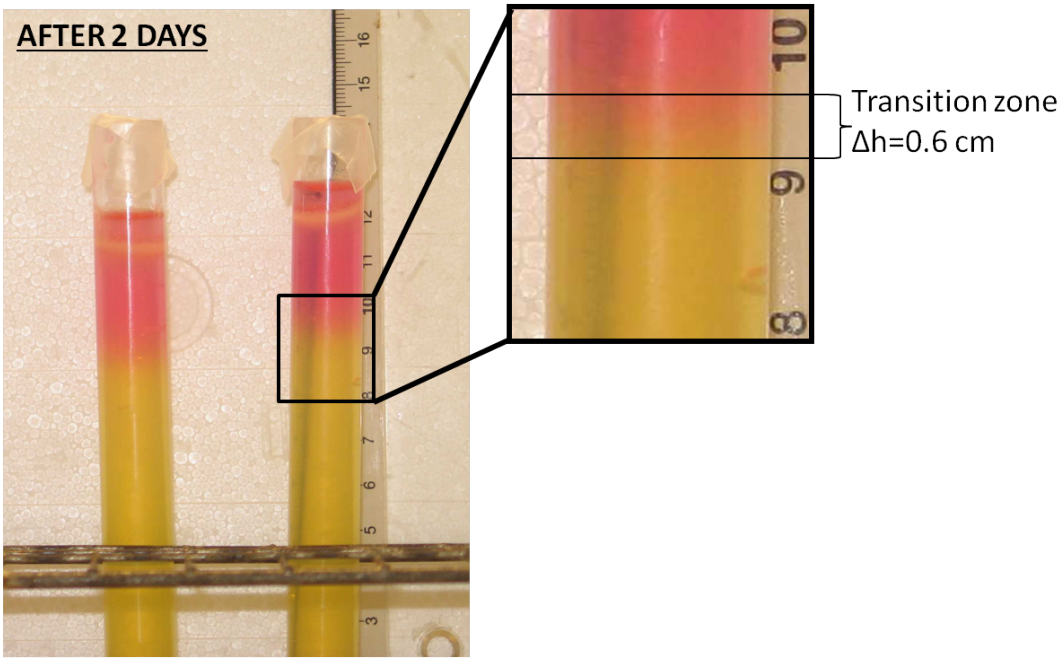


Figure 5.1: Errors in color change measurement (Provided by van Paassen)

The comparison between numerical simulation results and measured experimental data is given in Figure 5.2. It clearly illustrates that the model simulation agrees with the experimental observations. Discrepancies are mainly found in the range of 0.2 d to 2.0 d.

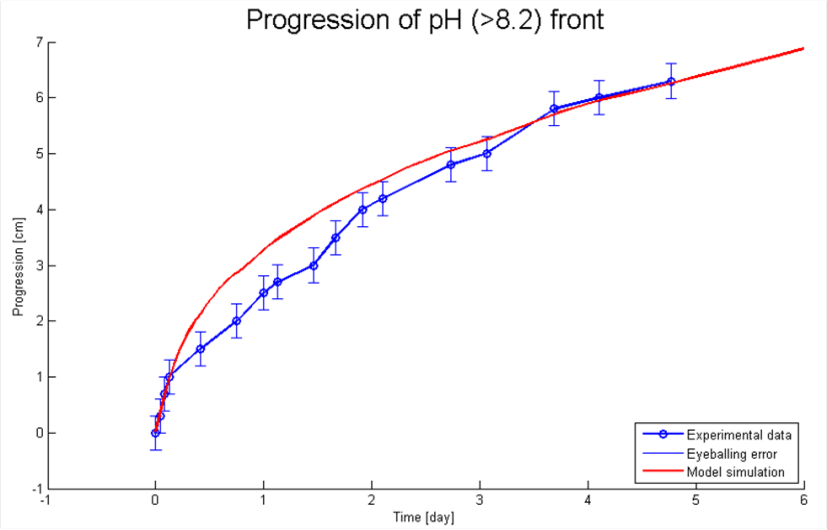


Figure 5.2: Comparison between experimental observation and model simulation result

Figure 5.3 shows the progress of urea hydrolysis process. Urea hydrolysis produces CO_3^{2-} and NH_4^+. On the one hand, produced CO_3^{2-} reacts with present Ca^{2+} and leads to calcite precipitation; on the other hand, produced CO_3^{2-} and NH_4^+ cause the local pH rise. The supply of CO_3^{2-} and NH_4^+ from urea hydrolysis and diffusion result in the pH $>$ 8.2 front advancement

towards the opposite boundary. In this simulation, the hydrolysis of urea is subjected to Monod kinetics, the depletion of urea at the upper boundary lowers the availability of urea and slows down the hydrolysis process as well as the supply of CO_3^{2-} and NH_4^+. As a consequence, the speed of observed pH $>$ 8.2 front progressively decreases as shown in Figure 5.3 the time required for the front to advance equal distance is increasing.

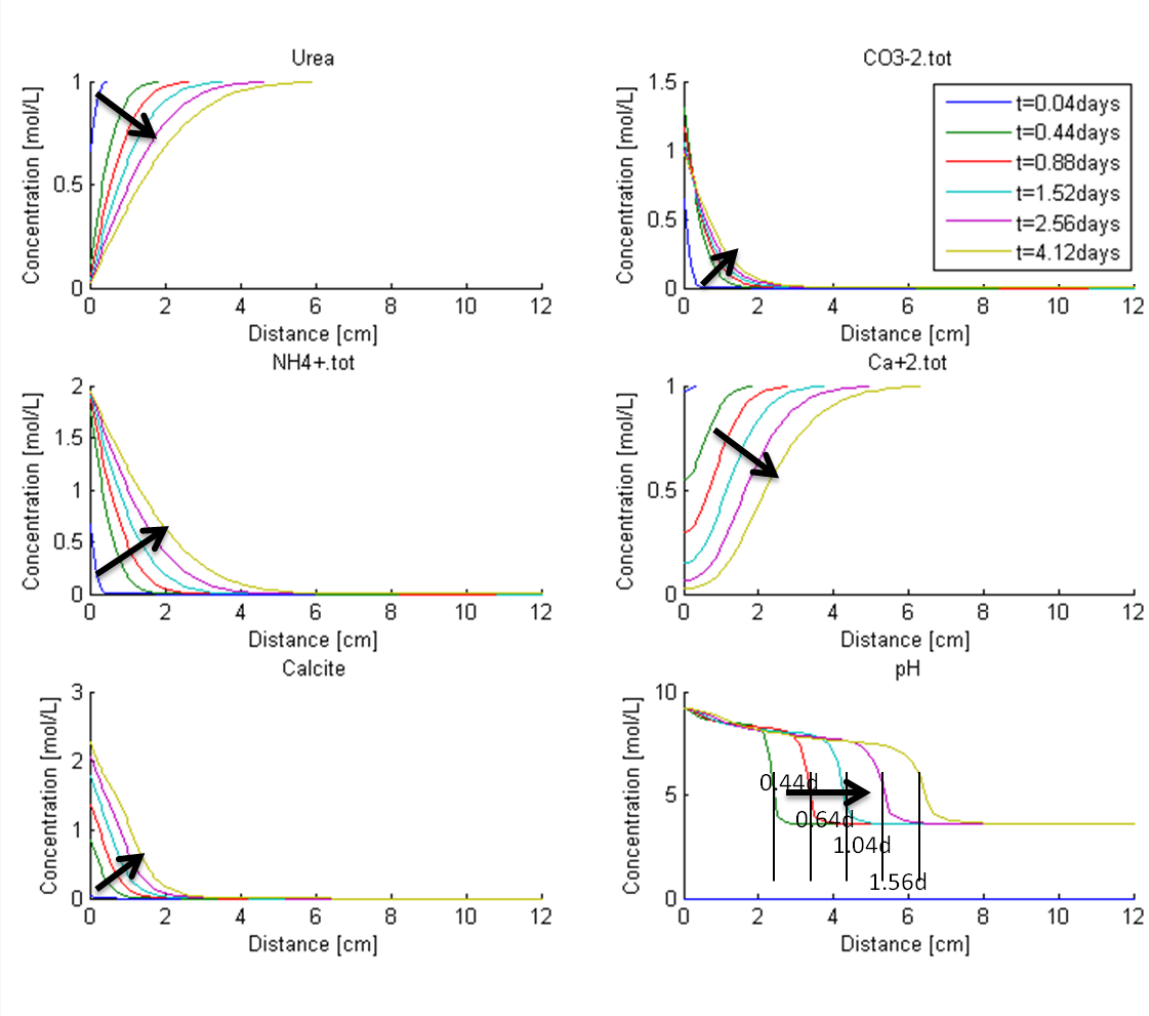


Figure 5.3: Progress of urea hydrolysis (arrows indicate changes over time)

In terms of measurement errors, these dependencies in the range of 0.2 d to 2.0 d are attributed to: 1) Although the error bar accounting for the color transition zone is included, the dimension of this zone is not constant over time and the eyeballing measurement contains significant amount of uncertainties; 2) The sensitivity of the phenol to the pH variations is unknown, there might be lagging time in the color change.

In terms of simulation errors, these dependencies are attributed to: 1) The diffusion coefficient of the gel is not calibrated, as discussed above, the progression of pH $>$ 8.2 front heavily relies on diffusion. Ideally the diffusion coefficient should be measured by dye diffusion test

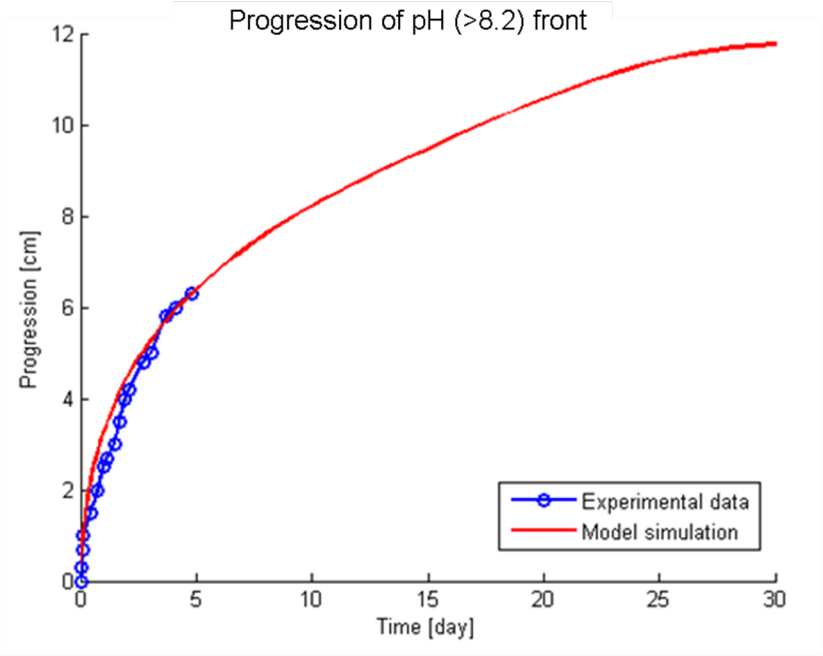


Figure 5.4: Simulated pH limit progression after 30 days

instead of extrapolated from literature; 2) The other driving force of the pH $>$ 8.2 front progression is the hydrolysis of urea. This simulation necessarily simplifies the microbially catalyzed urea hydrolysis kinetics as Monod kinetics; 3) The rate values for calcite precipitation are not calibrated, the removal of CO_3^{2-} via precipitation is important for the local pH; 4) The gas transfer as well as the alteration of transport medium properties are not included.

In Figure 5.4, we present result where we use the model to extrapolate the outcome of the experiment to long time (30 days). It takes 27.4 days before the while domain turns pink.

5.2 Calcite precipitation simulation

The experimental observations of c7uu provided by Gebrehiwet, et al., (2014) indicate the width of precipitated calcite zone is approximately 2.2 cm where precipitated calcite is visualized as white particles in the transparent transport medium. In addition, Gebrehiwet, et al., (2014) also present their simulation results in which the spatial distribution of calcite and porosity are given.

Figure 5.5 gives the comparison of our simulation results with Gebrehiwet, et al., (2014) experimental observations and simulations. The two red dash lines indicate the calcite precipitation zone and the black dash line is used to identify the densest calcite precipitation position. Comparing with their simulation work, our simulation results show greater match with the experimental observations where both the width and the position of precipitated calcite zone predicted by our model are consistent with the experimental observations.

The distribution of calcite predicted by our model deviates from the other simulation. This

might because our model adopts different rate law to express the calcite precipitation and our transport equation explicitly takes the tortuosity and porosity alterations into account. As a consequence, our simulation is comparably more realistic and the simulation results are more close to the experimental observations.

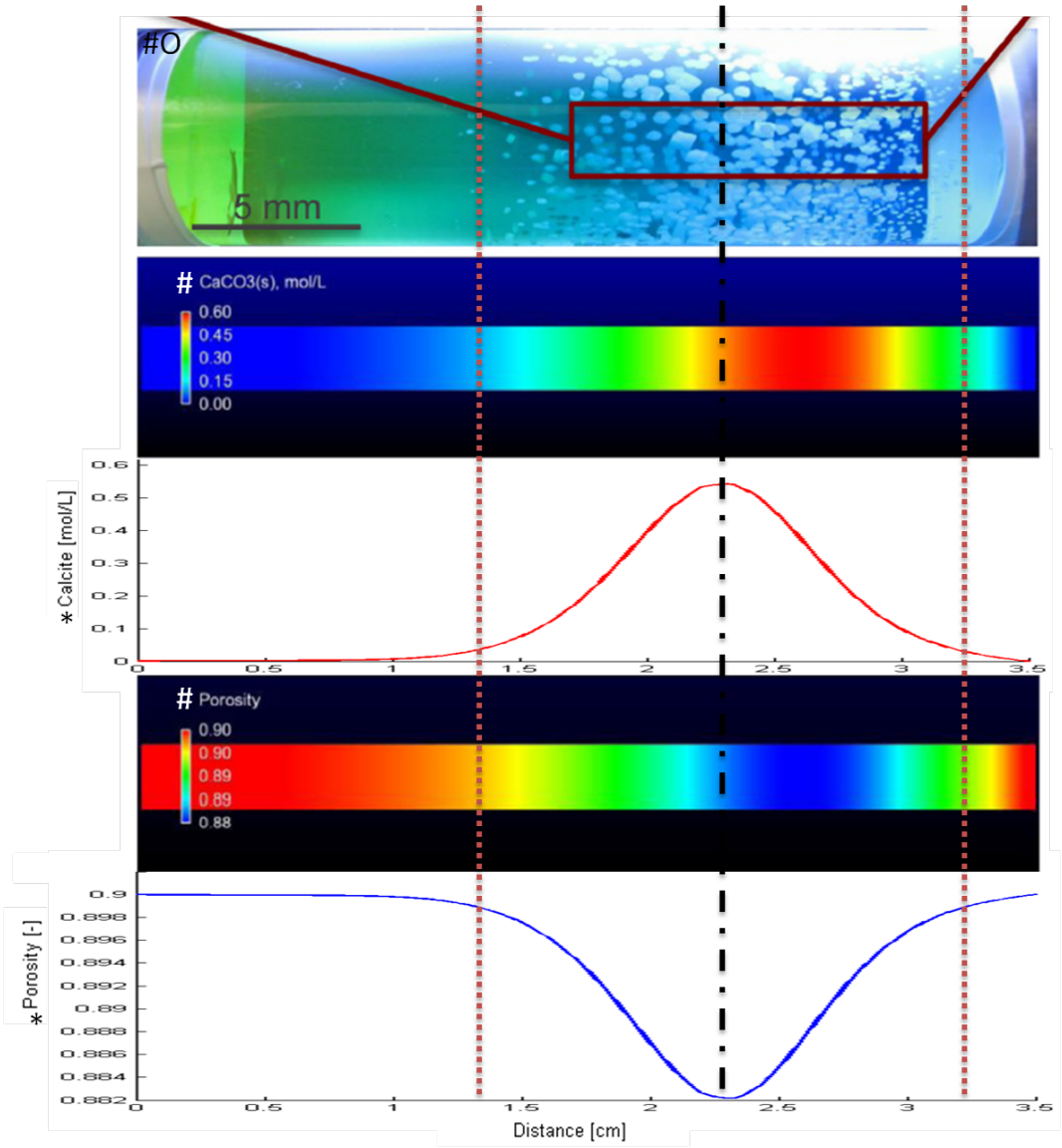


Figure 5.5: Simulation results and experimental observation for the calcite precipitation
Symbol '*' indicating simulation results from our model; symbol '#' denoting simulation results from Gebrehiwet, et al., (2014); symbol '#O' denoting experimental observation from Gebrehiwet, et al., (2014)

Asymmetry in calcite precipitation is observed, where calcite precipitates close to the bicarbonate boundary. As indicated by Gebrehiwet, et al., (2014), this might be related to the pH distribution. The availability of calcium and bicarbonate as well as pH distribution as a function of time and distance is presented in Figure 5.6. As shown in Figure 5.6, in this double diffusion configuration, the pH at the bicarbonate boundary is maintained at 9 while at the calcium side

the pH is kept at 7. According to the stoichiometry of calcite formation, the precipitation of calcite from bicarbonate consumes carbonate and releases protons. Hence, calcite precipitation decreases the local pH rise due to the supply of bicarbonate near the boundary. Meanwhile, released protons lower the pH in vicinity of the calcium boundary. In other words, the calcite precipitation process intensifies the asymmetric pH distribution. A higher pH close to the bicarbonate side leads to the conditions that are more favorable for calcite to reach its supersaturation state, and as a consequence, more calcite precipitates.

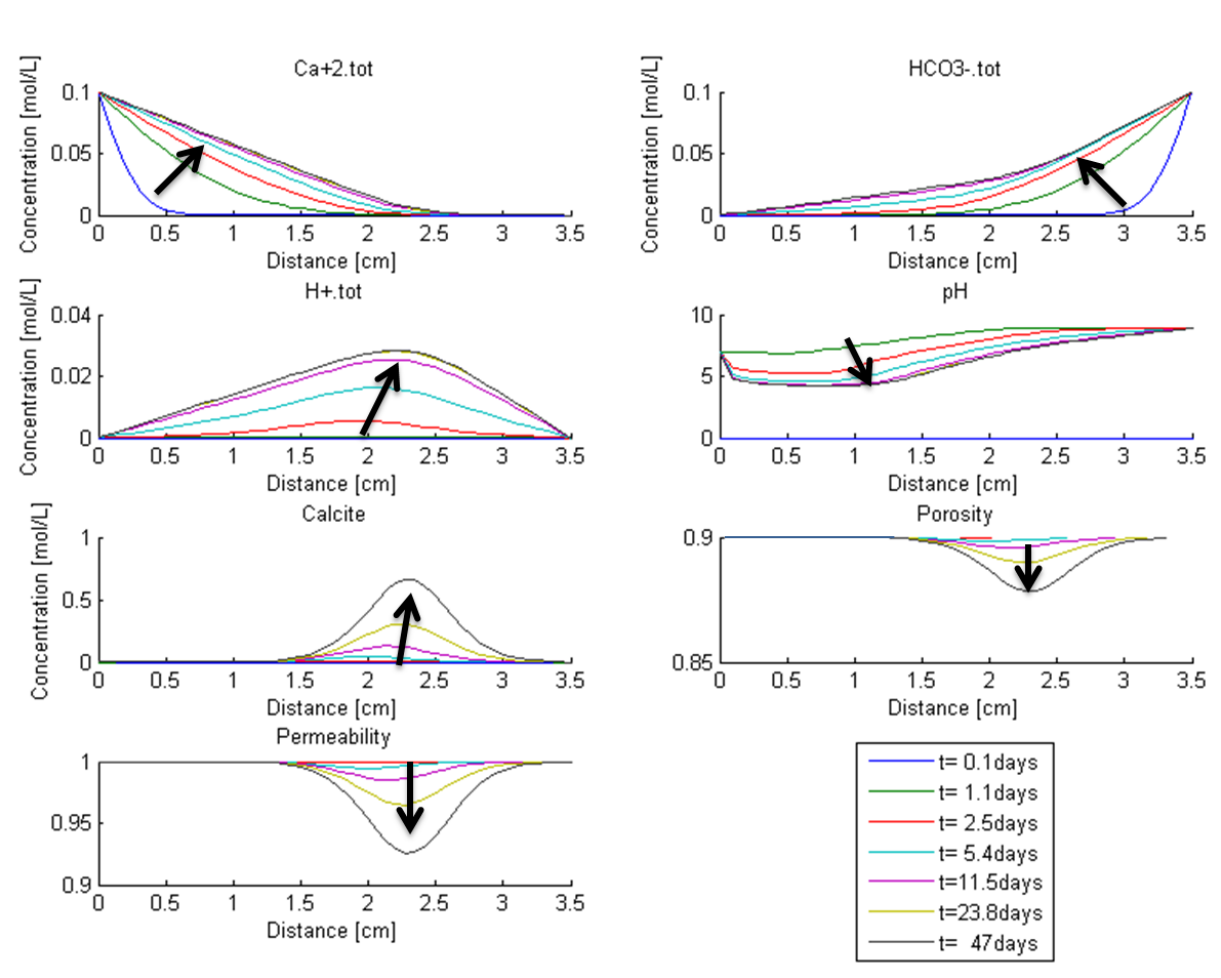


Figure 5.6: Progress of calcite precipitation under double diffusion control (arrows indicate changes over time)

5.3 Microbially influenced mineral precipitation simulation

In this Subsection, simulations results of a system which includes sulfate reducing bacteria in a counter diffusion set-up of sulfate and ferrous iron are presented. In Subsection 5.3.1, simulation results of varying boundary sulfate concentration (S series) and varying boundary ferrous iron concentration (F series) are given respectively. Simulation results of changing distance are presented in Subsection 5.3.3

5.3.1 Varying boundary concentrations

5.3.1.1 Varying sulfate boundary concentrations

Figure 5.7 and Figure 5.8 present the simulation results after 30 days for scenarios with varying boundary sulfate concentrations. In the low boundary $C_{SO_4^{2-}}$ case (series S1), the low availability of sulfate limits the growth of biomass. Consequently, the biomass is mainly under decay except at the sulfate boundary, where biomass has the access to sulfate in order to maintain growth and produce metabolites. These released metabolites, hydrogen sulfide and bicarbonate, cause minerals to precipitate once supersaturated. Limited by the supply of sulfate, the rate of HS^- production is relatively low compared with pyrrhotite precipitation rate. Hence, HS^- is rapidly consumed due to the fast precipitation of pyrrhotite in vicinity of the sulfate boundary. Although the rate of HCO_3^- production is low as well, the relatively high solubility product of siderite makes it comparably difficult for siderite to reach its supersaturation state. Therefore, HCO_3^- has larger chance to diffuse away and precipitate as siderite at the higher ferrous iron concentration site. Because the occurrence of pyrrhotite precipitation releases protons near the sulfate boundary, it causes a gradual pH decline moving away from the sulfate boundary as shown in Figure 5.8.

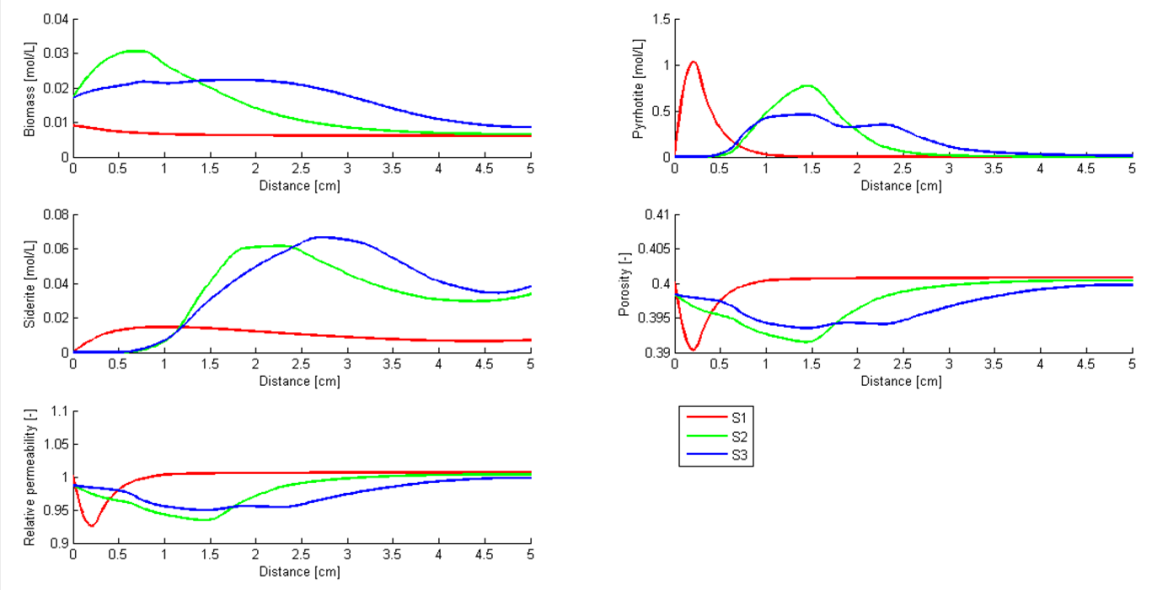


Figure 5.7: Solid mass accumulation and transport properties regarding various boundary sulfate concentrations after 30 days

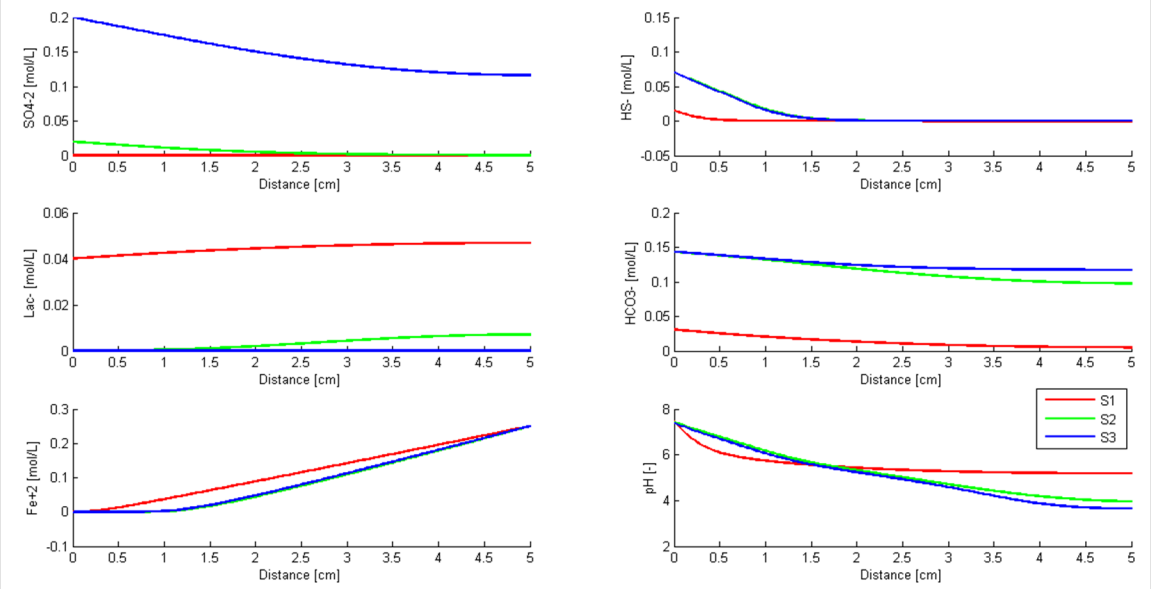


Figure 5.8: Aqueous species profile regarding various boundary sulfate concentrations after 30 days

In terms of high sulfate concentrations at the boundary, biomass growth is no longer limited especially HCO_3^- is present at much higher concentration, and as such both pyrrhotite and siderite are supersaturated. HCO_3^- diffuses much further than HS^- due to the higher siderite solubility product compared with pyrrhotite. As a result, precipitation occurs closer to the iron corrosion boundary.

In the simulation results of S3, the pyrrhotite precipitation indicates the presence of double zonation. This interesting phenomenon can be attributed to the biomass growth kinetics. Figure 5.9 and 5.10 present a time series of the aqueous species profile and solid mass accumulation of series S3. The series S3 is a scenario for an engineered sulfate boundary concentration situation, where sulfate is assumed to be abundant. Sulfate gradually diffuses towards the reaction region and activates the biomass growth. Due to the prevention of iron surface, abundant sulfate entered from the sulfate boundary quickly accumulates inside the reaction region. With high availability of both sulfate and lactate, biomass forms at a relatively high rate, which we call the first biomass growth stage. As a result, HS^- has a high production rate and precipitates with Fe^{2+}, which diffused from the iron corrosion boundary, to approximately 2.4 cm away from the sulfate boundary after 3 days as the green line indicates in Figure 5.10. The first growth stage lasts for 10 days until lactate is depleted. The HS^- released along the first growth stage leads to the formation of pyrrhotite zone 1, which is signified as $Z1$ in Figure 5.9. After 10 days, the biomass starts to decay and no more HS^- is produced, this phase is called second growth stage. The remaining HS^- from the first growth stage is continuously consumed by pyrrhotite precipitation. The decrease in HS^- is controlled by the continuing increase of Fe^{2+} shifting the position of pyrrhotite precipitation backwards to the sulfate boundary and leading to the formation of pyrrhotite zone 2, $Z2$.

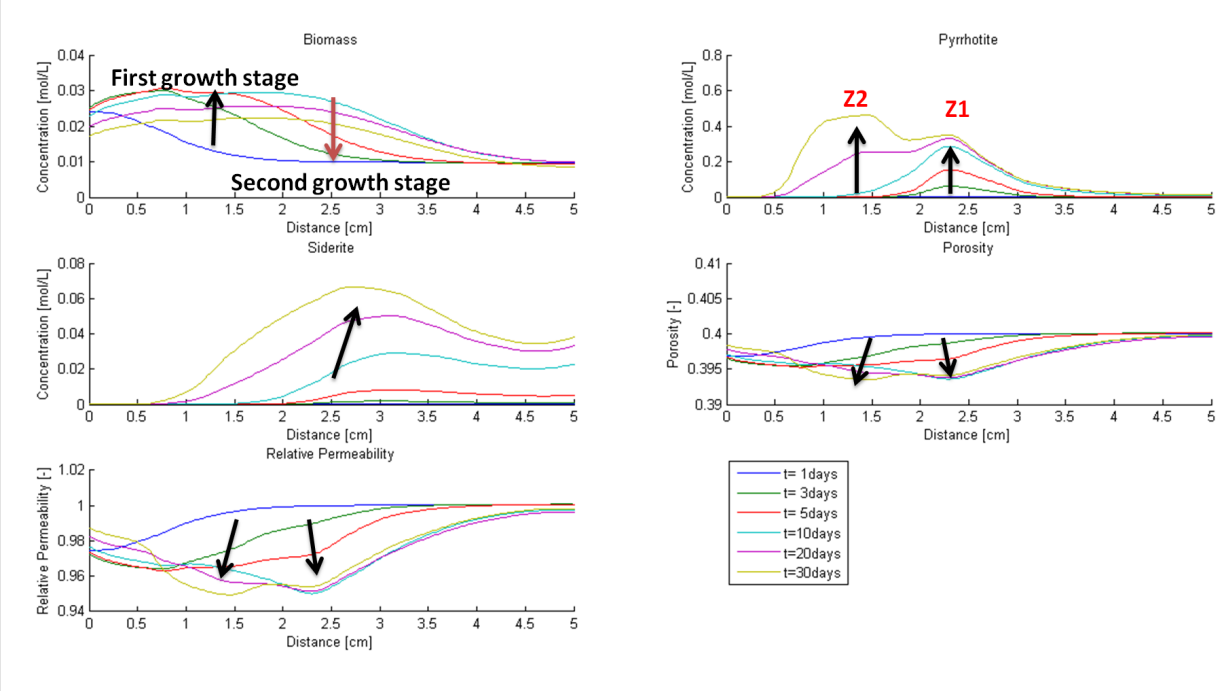


Figure 5.9: Progress of solid mass accumulation and transport properties changes in series S3 (arrows indicate changes over time)

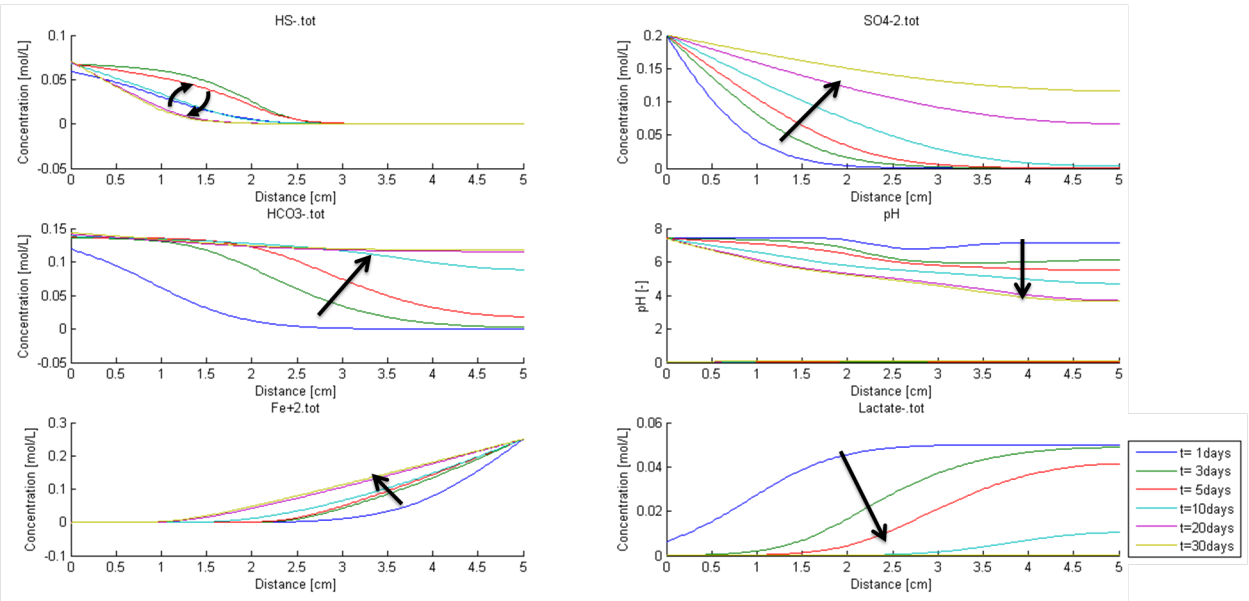


Figure 5.10: Progress of aqueous species concentration changes in series S3 (arrows indicate changes over time)

Siderite does not show the double zonation phenomenon which can be explained by the high solubility product of siderite which significantly slows down the siderite precipitation. In other

words, the HCO_3^- released from the first biomass growth stage is present at relatively high concentration and keeps the precipitation front of siderite at more or less the same position.

5.3.1.2 Varying iron corrosion rates

Figure 5.11 and Figure 5.12 show the simulation results after 30 days for scenarios with varying corrosion rates. According to these simulation results, the corrosion rate has little impact on the growth of biomass. This is reasonable since the biomass formation kinetics are only controlled by the availability of sulfate and lactate, where both are set as invariants in the varying corrosion rates series. The varying corrosion rates significantly affect the spatial distribution of iron precipitates. With increasing corrosion rate, the pyrrhotite precipitation zone moves closer to the sulfate boundary with reducing width and increasing magnitude. The rationale behinds this migration can be concluded as the asymmetry of boundary reactants concentrations. The higher solute concentration boundary induces a sharper concentration gradient, and a sharper gradient allows ions to travel further and faster. As a consequence, ions diffused from the higher solute concentration boundary meet the opposing reactants in the vicinity of the lower solute concentration boundary.

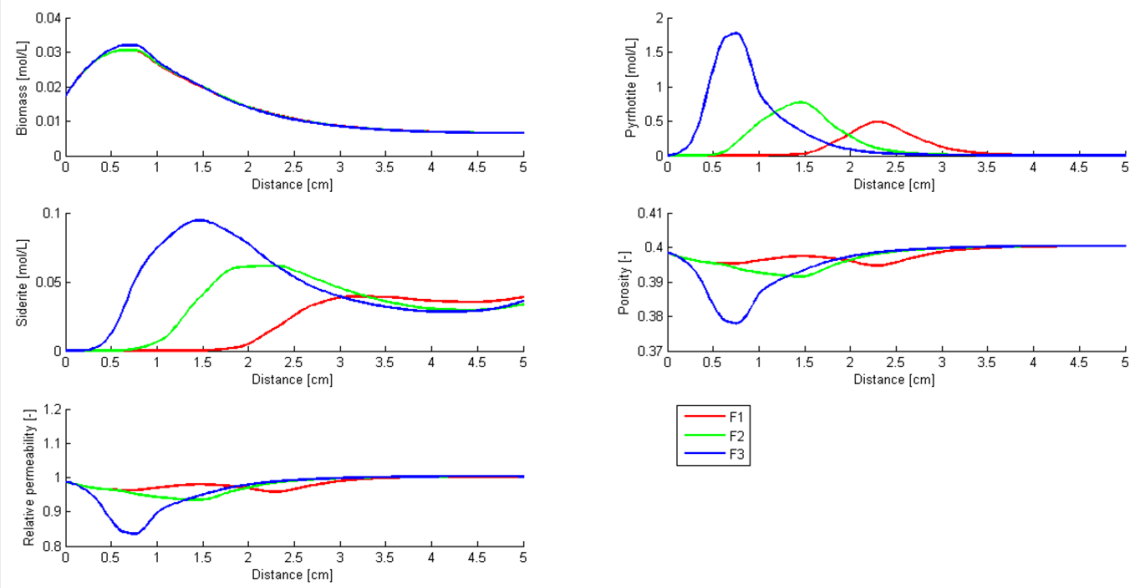


Figure 5.11: Solid mass accumulation and transport properties regarding varying corrosion rates after 30 days

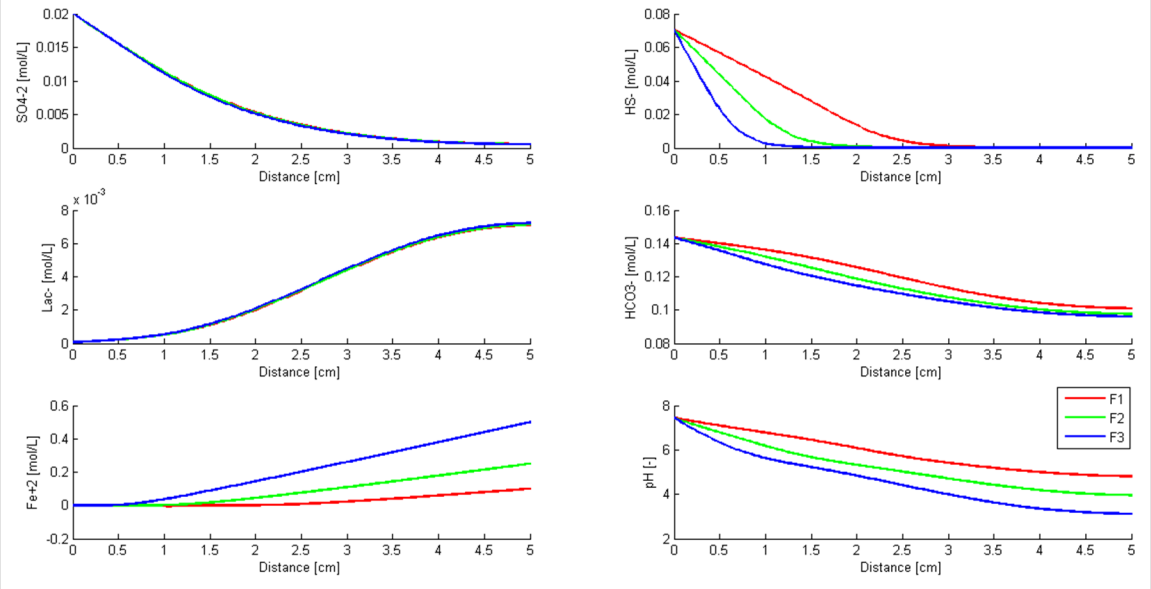


Figure 5.12: Aqueous species profile regarding varying corrosion rates after 30 days

With increasing iron corrosion rates, the amount of precipitated siderite is actually reducing in vicinity to the iron corrosion boundary. As stated in Paragraph 2.1.1.2, the solubility of siderite increases dramatically with drops in local pH. The accelerated dissolution of siderite under low pH conditions leads to less siderite precipitating near the iron corrosion boundary.

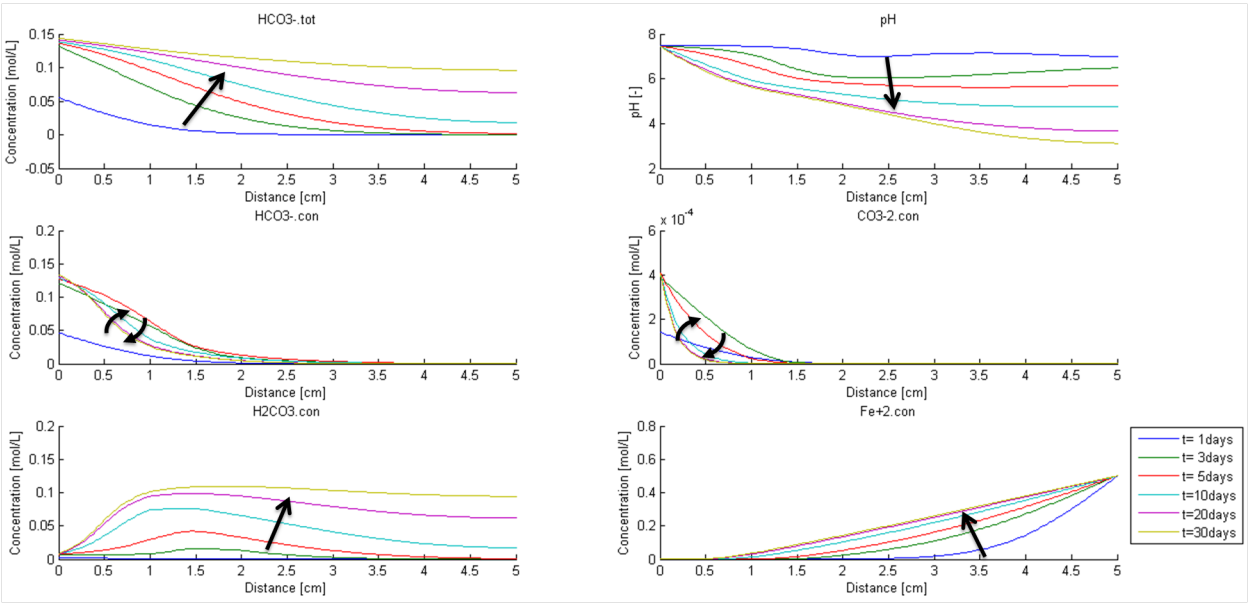


Figure 5.13: pH development and carbonic acid speciation process in F3 series (arrows indicate changes over time)

Although we have not explicitly taken the stability of minerals into account, as mentioned in Subsection 2.4.3, it is implicitly included in the speciation of reference states. Figure 5.13

presents the relation between pH development and carbonic acid speciation process. The *TIC* is increasing with the ongoing lactate consumption and biomass growth while the lowering pH makes H_2CO_3 gradually become the dominant species. The observed reduction in siderite precipitates near the iron corrosion boundary leads to the conclusion that the stability of minerals is partially governed by the pH-dependent speciation.

5.3.2 Effects of varying boundary concentrations

The varying boundary concentrations directly govern the position and magnitude of solid mass accumulation in microbially influenced mineral precipitation process. According to these simulation results presented above, the relatively high concentration at one boundary drives the accumulation of solid mass toward the opposing boundary. It should be clarified that the high concentration defined here is relative, it is more related to the ratio between the two boundary concentrations. In terms of high sulfate boundary concentrations (such as the series S3 in Paragraph 5.3.1.1) the maximum porosity reduction is relatively low but occurs over a wider range, from 0.75 cm to 3.5 cm. In the F3 series, after 30 days the maximum porosity reduction is about 6% and 0.75 cm away from the sulfate recharge boundary.

For corrosion prevention purposes, the S3 simulation results provide some insights. The engineered sulfate recharge boundary helps to form a barrier, which is mainly composed by biomass and pyrrhotite. With adequate time, the barrier could possibly block the pores and cut off the diffusive flux of ferrous iron.

5.3.3 Varying distances

Figure 5.14 and Figure 5.15 show the simulation results after 30 days for scenarios with varying distances. As already discussed in the interpretation of the simulation results of the series F, the biomass growth only depends on sulfate, lactate and ammonium. Therefore, varying distance has little effect on the biomass growth and subsequent biomass distribution. The main effect of varying distance is on the spatial distribution of aqueous species. With an increment in the distance, these aqueous species are spread over a wider range with reducing local availability. Decreasing availability of reactants make the establishment of supersaturation more difficult. Consequently, the magnitude and the rate of mineral precipitation are greatly reduced as shown in Figure 5.16. In the L3 series, the amount of precipitated pyrrhotite and siderite are almost negligible.

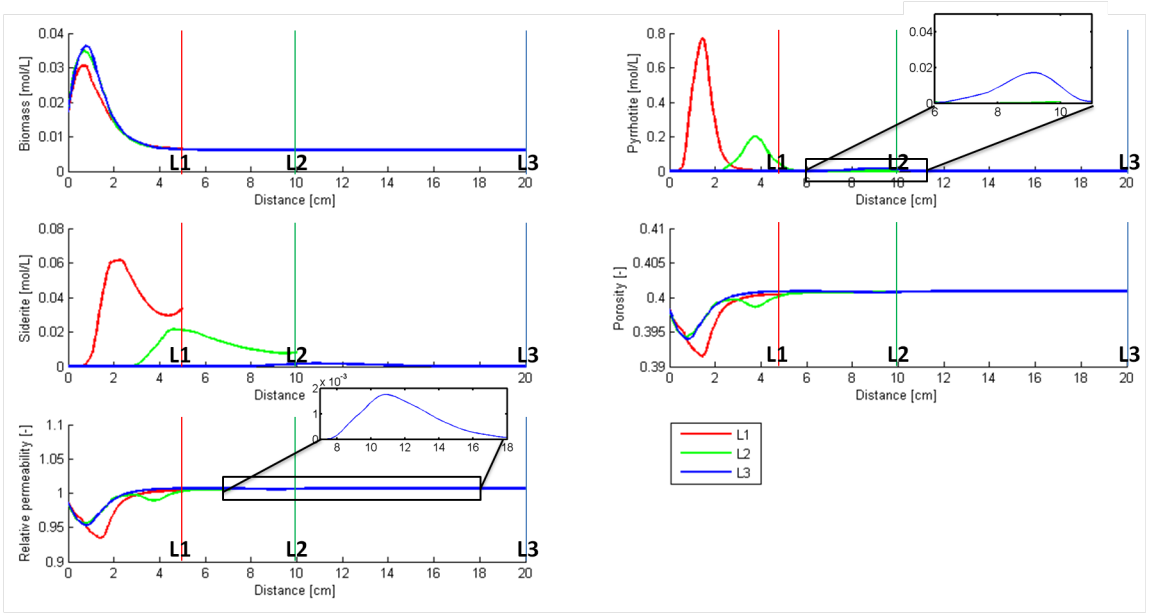


Figure 5.14: Solid mass accumulation and transport properties regarding varying distances after 30 days

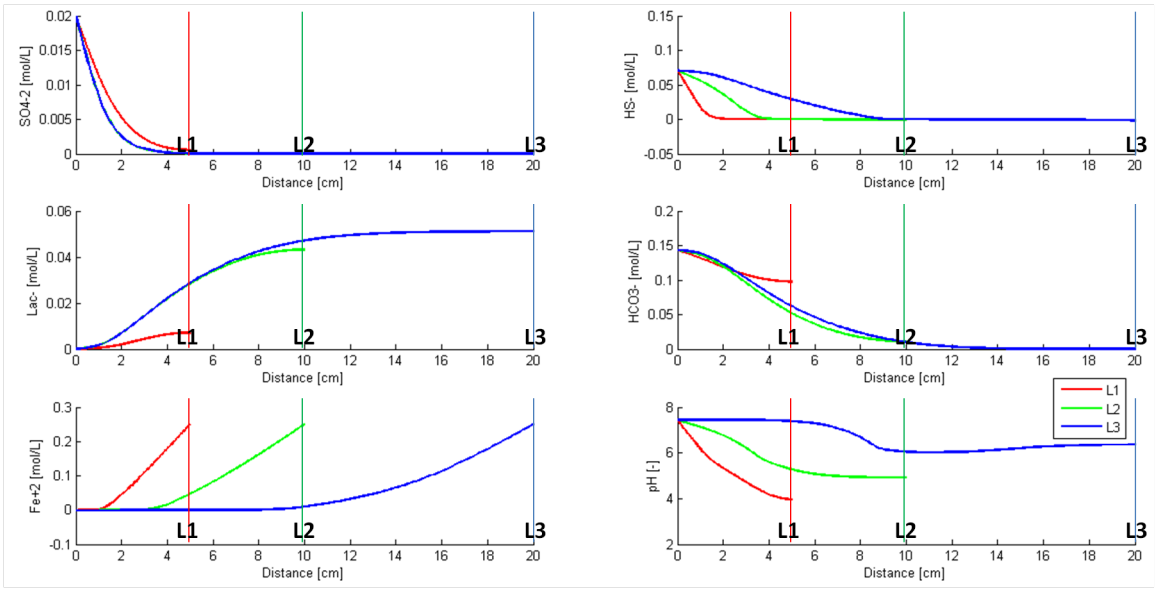


Figure 5.15: Aqueous species profile regarding varying distances after 30 days

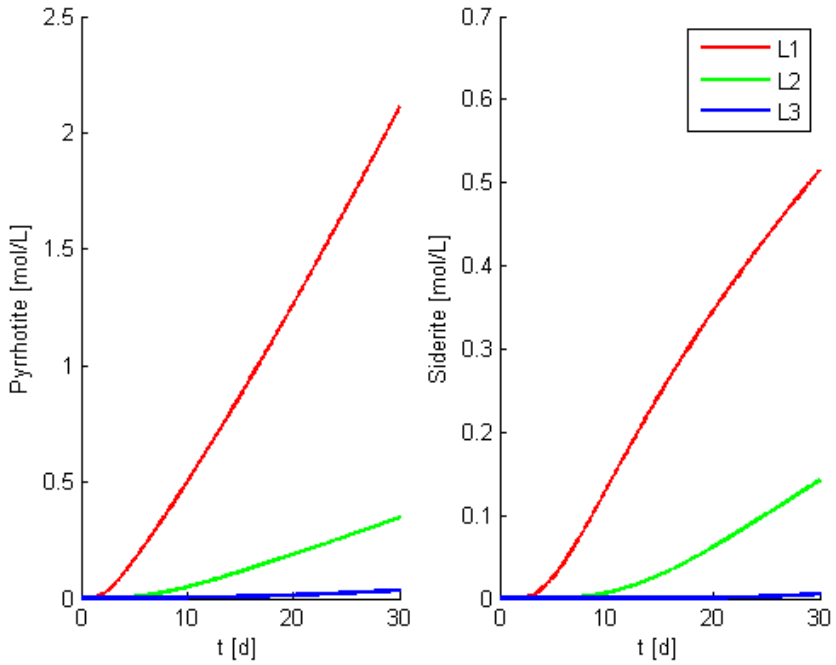


Figure 5.16: Cumulative iron mineral precipitation in L series

5.3.4 Effects of varying distances

The increasing distance dramatically lowers the magnitude of mineral precipitation as shown in Figure 5.14, while the biomass forms near the sulfate recharge boundary, approximately 2 cm away. The increasing distance greatly dilutes the effects of microbial activities on the mineral precipitation, as well as the permeability reduction around the iron corrosion boundary. According to the simulation results, almost no detectable permeability reduction is observed in vicinity to the iron corrosion boundary.

In terms of iron corrosion prevention measures via the injection of sulfate, in order to achieve expected solid mass barrier, the injection site shouldn't be too far away from the iron corrosion site.

5.4 Effects of varying precipitation rates

This research assumes mineral precipitation to occur when supersaturation is reached. In terms of first order kinetics, three parameters are required. They are the solubility product (K_M), precipitation rate (k_1) and dissolution rate (k_2). The value of solubility product is well-known for most commonly known minerals. However, the precipitation rate and dissolution rate are normally adjusted to fit specific case studies and their values could vary over several orders of magnitude (Hunter et al., 1998). In order to test the effects of varying rate values on the mineral precipitation simulation, the same set-up for calcite precipitation under the double diffusion is

used, in which the precipitation rate values are varied. The dissolution rate and solubility product are set as invariants.

Figure 5.17 gives the comparison of the simulated calcite precipitation with various precipitation rates. The datum k_1 is the precipitation rate used in the calcite precipitation simulation. This comparison covers three orders of magnitude. The results clearly indicate that the position of the maximum calcite precipitation zone is not affected by the precipitation rate, but the width of calcite precipitation zone reduces accordingly with increasing precipitation rates. The width variations can be explained: in case of high k_1 the fast removal of reactants which limits the spatial migration of reactants leads to a narrow accumulation of precipitated mineral.

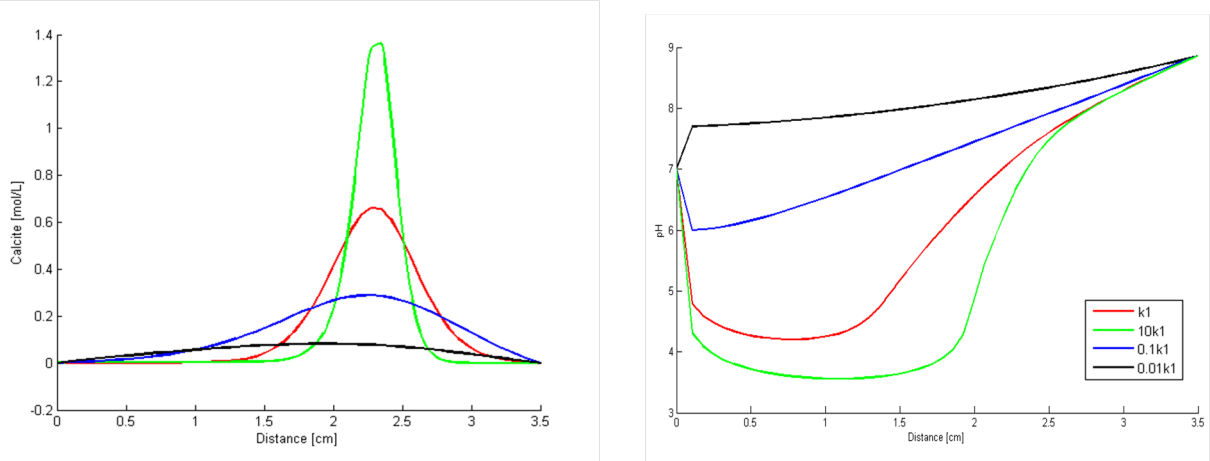


Figure 5.17: The simulated calcite precipitation with various precipitation rates after 47 days

The non-affected maximum calcite accumulation position might not be a common observation. Figure 5.17 also presents the pH profile associated with various precipitation rates. The formation of calcite from HCO_3^- releases protons and induces a local drop in pH. Under the high k_1 circumstance, indicated by the green line, the pH can drop below 4. Due to the fact that the analyzed precipitation process here is relatively simple, in which no microbial activities are included and only one type of minerals is considered, the effects of high acidity are not profound yet. Nevertheless, if the system consists of multiple kinetic processes, the resulted acidity will greatly affect the overall kinetics and lead to a shift in the position of maximum precipitation. One example is the reducing amount of siderite near the iron corrosion boundary as shown in Figure 5.11.

6 Summary and conclusions

This model includes a relatively wide range of processes, which enables a more comprehensive representation of complex interactions in the subsurface environment. In terms of biomass development, this model includes the sequential degradation of electron donors, sequential utilization of electron acceptors, kinetic biomass growth and decay. The geochemical reaction module is constructed considering the time-scale of reactions, in which both kinetic reactions and equilibrium reactions are explicitly included. In the representation of transport process, only diffusion under fully saturated condition is considered, the physical transport medium properties in this model are interconnected with bio-chemical reactions. In a conclusion, this model has profoundly investigated these three dominating processes and their interactions.

Series of simplifications and assumptions were made. The biofilm dynamics are ignored which results the localized simulated biomass distribution. In terms of mineral precipitation, this model applies a uniform rate law for all minerals. It leads to a generic expression but also might oversimplify the kinetics regarding specific mineral precipitation processes. Although this model presents the possibility of the inclusion of gas phase, all simulations are implemented with the fully saturation assumption.

The model has been verified using experimental data from two different experiments, and proven to be able to give accurate predictions. Nevertheless, the verification does not cover the entire model yet. The sequential degradation of electron donors, sequential utilization of electrons and the gas-liquid equilibrium modules have not been verified. Their effects on microbially influenced mineral precipitation are not investigated.

In the application of this model on microbially influenced mineral precipitation simulation, this model helps to predict the effects of varying boundary concentrations and varying distance on the spatial distribution of precipitated minerals. 1) In terms of mineral precipitation under double diffusion control, precipitation mainly occurs close to the low concentration boundary; 2) Precipitation position and magnitude are highly influenced by the solubility product of minerals. The solubility product helps to study the competition for species among various minerals; 3) Microbial activities influence the concentrations of species and therefore drive mineral precipitation; 4) Although this research does not specifically investigate a microbially driven siderite precipitation strategy under sulfate reduction condition, it can be possibly achieved by preventing pH from reducing in the vicinity of iron surface.

Acknowledge

The author thanks Timo J. Heimovaara, Michael Afanasyev and André G. van Turnhout for their assistance with the model development and report writing. Thanks André G. van Turnhout for the MATLAB-ORCHESTRA interface construction, and Michael Afanasyev for his kind supervisions in terms of scenario confirmation, and van Paassen, L. A for the provision of urea hydrolysis experimental data.

References

[1] Al-Darbi, M. M., Agha, K., & Islam, M. R. (2005). Comprehensive modelling of the pitting biocorrosion of steel. The Canadian Journal of Chemical Engineering, 83(5), 872-881.

[2] Appelo, C. A. J., & Postma, D. (2005). Geochemistry, groundwater and pollution. CRC Press.

[3] Baedecker, M. J., & Back, W. (1979). Modern marine sediments as a natural analog to the chemically stressed environment of a landfill. Developments in Water Science, 12, 393-414.

[4] Banfield, J. F., Barker, W. W., Welch, S. A., & Taunton, A. (1999). Biological impact on mineral dissolution: application of the lichen model to understanding mineral weathering in the rhizosphere. Proceedings of the National Academy of Sciences, 96(7), 3404-3411.

[5] Barry, D. A., Parlange, J. Y., & Hensley, P. J. (1993). Calculation of kinetic rate constants from steady-state soil profile concentration measurements. International Journal for Numerical and Analytical Methods in Geomechanics, 17(4), 243-254.

[6] Battley, E. H. (1987). Energetics of microbial growth.

[7] Bear (1972). Dynamics of Fluids in Porous Media. Dover.

[8] Bear (1979). Hydraulics of Groundwater. Dover.

[9] Beech, I. B., & Gaylarde, C. C. (1999). Recent advances in the study of biocorrosion: an overview. Revista de microbiologia, 30(3), 117-190.

[10] Beech, I. B., & Sunner, J. (2004). Biocorrosion: towards understanding interactions between biofilms and metals. Current opinion in biotechnology,15(3), 181-186.

[11] Belay, N., & Daniels, L. (1990). Elemental metals as electron sources for biological methane formation from CO2. Antonie van leeuwenhoek, 57(1), 1-7.

[12] Biezma, M. (2001). The role of hydrogen in microbiologically influenced corrosion and stress corrosion cracking. International Journal of Hydrogen Energy, 26(5), 515-520.

[13] Bjerg, P. L., Ruegge, K., Pedersen, J. K., & Christensen, T. H. (1995). Distribution of redox-sensitive groundwater quality parameters downgradient of a landfill (Grindsted, Denmark). Environmental science & technology,29(5), 1387-1394.

[14] Bose, A., Gardel, E. J., Vidoudez, C., Parra, E. A., & Girguis, P. R. (2014). Electron uptake by iron-oxidizing phototrophic bacteria. Nature communications, 5.

[15] Borden, R. C., & Bedient, P. B. (1986). Transport of dissolved hydrocarbons influenced by oxygen-limited biodegradation: 1. Theoretical development. Water Resources Research, 22(13), 1973-1982.

[16] Borden, R. C., Bedient, P. B., Lee, M. D., Ward, C. H., & Wilson, J. T. (1986). Transport of dissolved hydrocarbons influenced by oxygen-limited biodegradation: 2. Field application. Water Resources Research, 22(13), 1983-1990.

[17] Bottero, S., Storck, T., Heimovaara, T. J., van Loosdrecht, M. C., Enzien, M. V., & Picioreanu, C. (2013). Biofilm development and the dynamics of preferential flow paths in porous media. Biofouling, 29(9), 1069-1086.

[18] Boudreau, B. P., Meysman, F. J., & Middelburg, J. J. (2004). Multicomponent ionic diffusion in porewaters: Coulombic effects revisited. Earth and Planetary Science Letters, 222(2), 653-666.

[19] Bourdoiseau, J. A., Jeannin, M., Rémazeilles, C., Sabot, R., & Refait, P. (2011). The transformation of mackinawite into greigite studied by Raman spectroscopy. Journal of Raman Spectroscopy, 42(3), 496-504.

[20] Chan, E. W. L. (2011). Magnetite and its galvanic effect on the corrosion of carbon steel under carbon dioxide environments.

[21] Clement, T. P., Hooker, B. S., & Skeen, R. S. (1996). Macroscopic models for predicting changes in saturated porous media properties caused by microbial growth. Groundwater, 34(5), 934-942.

[22] Cole, I. S., & Marney, D. (2012). The science of pipe corrosion: A review of the literature on the corrosion of ferrous metals in soils. Corrosion science, 56, 5-16. Chicago

[23] Cord-Ruwisch, R. (2000). Microbially influenced corrosion of steel.

[24] Corey (1994). Mechanics of Immiscible Fluids in Porous Media. Water Resources Publications.

[25] Daniels, L., Belay, N., Rajagopal, B. S., & Weimer, P. J. (1987). Bacterial methanogenesis and growth from CO2 with elemental iron as the sole source of electrons. Science, 237(4814), 509-511.

[26] de Romero, M., Duque, Z., Rodríguez, L., de Rincón, O., Pérez, O., & Araujo, I. (2005). A study of microbiologically induced corrosion by sulfate-reducing bacteria on carbon steel using hydrogen permeation. Corrosion, 61(1), 68-75.

[27] Enning, D., & Garrelfs, J. (2014). Corrosion of iron by sulfate-reducing bacteria: new views of an old problem. Applied and environmental microbiology, 80(4), 1226-1236.

[28] Enning, D., Venzlaff, H., Garrelfs, J., Dinh, H. T., Meyer, V., Mayrhofer, K., ... & Widdel, F. (2012). Marine sulfate-reducing bacteria cause serious corrosion of iron under electroconductive biogenic mineral crust. Environmental microbiology, 14(7), 1772-1787.

[29] Fennell, D. E., & Gossett, J. M. (1998). Modeling the production of and competition for hydrogen in a dechlorinating culture. Environmental Science & Technology, 32(16), 2450-2460.

[30] Gorby, Y. A., Yanina, S., McLean, J. S., Rosso, K. M., Moyles, D., Dohnalkova, A., ... & Fredrickson, J. K. (2006). Electrically conductive bacterial nanowires produced by Shewanella oneidensis strain MR-1 and other microorganisms. Proceedings of the National Academy of Sciences, 103(30), 11358-11363.

[31] Gião, M. S., Montenegro, M. I., & Vieira, M. J. (2005). The influence of hydrogen bubble formation on the removal of< i> Pseudomonas fluorescens</i> biofilms from platinum electrode surfaces. Process Biochemistry, 40(5), 1815-1821.

[32] Habicht, K. S., Gade, M., Thamdrup, B., Berg, P., & Canfield, D. E. (2002). Calibration of sulfate levels in the Archean ocean. Science, 298(5602), 2372-2374.

[33] Hamilton, W. A. (2003). Microbially influenced corrosion as a model system for the study of metal microbe interactions: a unifying electron transfer hypothesis. Biofouling, 19(1), 65-76.

[34] Heijnen, J. J. (1999). Bioenergetics of microbial growth. Encyclopedia of Bioprocess Technology.

[35] Huang, P. M., Bollag, J. M., & Senesi, N. (Eds.). (2002). Interactions between soil particles and microorganisms: impact on the terrestrial ecosystem. John Wiley & Sons.

[36] Hunt, S. M., Werner, E. M., Huang, B., Hamilton, M. A., & Stewart, P. S. (2004). Hypothesis for the role of nutrient starvation in biofilm detachment. Applied and environmental microbiology, 70(12), 7418-7425.

[37] Hunter, K. S., Wang, Y., & Van Cappellen, P. (1998). Kinetic modeling of microbially-driven redox chemistry of subsurface environments: coupling transport, microbial metabolism and geochemistry. Journal of hydrology,209(1), 53-80.

[38] Islam, J., & Singhal, N. (2002). A one-dimensional reactive multi-component landfill leachate transport model. Environmental Modelling & Software, 17(6), 531-543.

[39] Javaherdashti, R. (2008). Microbiologically influenced corrosion: an engineering insight. Springer.

[40] Kato, S., Hashimoto, K., & Watanabe, K. (2012). Microbial interspecies electron transfer via electric currents through conductive minerals. Proceedings of the National Academy of Sciences, 109(25), 10042-10046.

[41] King, R. A., & Miller, J. D. A. (1971). Corrosion by the sulphate-reducing bacteria.

[42] King, R. A., Miller, J. D. A., & Wakerley, D. S. (1973). Corrosion of mild steel in cultures of sulphate-reducing bacteria: effect of changing the soluble iron concentration during growth. British Corrosion Journal, 8(2), 89-93.

[43] Konhauser, K. O. (1997). Bacterial iron biomineralisation in nature. FEMS Microbiology Reviews, 20(3-4), 315-326.

[44] Konhauser, K. O. (2009). Introduction to geomicrobiology. John Wiley & Sons.

[45] Kuang, F., Wang, J., Yan, L., & Zhang, D. (2007). Effects of sulfate-reducing bacteria on the corrosion behavior of carbon steel. Electrochimica Acta, 52(20), 6084-6088.

[46] Lovley, D. R., & Goodwin, S. (1988). Hydrogen concentrations as an indicator of the predominant terminal electron-accepting reactions in aquatic sediments. Geochimica et Cosmochimica Acta, 52(12), 2993-3003.

[47] MallaáShrestha, P. (2014). A new model for electron flow during anaerobic digestion: direct interspecies electron transfer to Methanosaeta for the reduction of carbon dioxide to methane. Energy & Environmental Science, 7(1), 408-415.

[48] Maxwell, S. (2006, January). Predicting microbially influenced corrosion in seawater injection systems. In SPE International Oilfield Corrosion Symposium. Society of Petroleum Engineers.

[49] McLean, J. S., Lee, J. U., & Beveridge, T. J. (2002). Interactions of bacteria and environmental metals, fine-grained mineral development and bioremediation strategies. IUPAC SERIES ON ANALYTICAL AND PHYSICAL CHEMISTRY OF ENVIRONMENTAL SYSTEMS, 8, 227-262.

[50] Monod, J. (1949). The growth of bacterial cultures. Annual Reviews in Microbiology, 3(1), 371-394.

[51] Mori, K., Tsurumaru, H., & Harayama, S. (2010). Iron corrosion activity of anaerobic hydrogen-consuming microorganisms isolated from oil facilities. Journal of bioscience and bioengineering, 110(4), 426-430.

[52] Nešic, S., Nordsveen, M., Nyborg, R., & Stangeland, A. (2003). A mechanistic model for carbon dioxide corrosion of mild steel in the presence of protective iron carbonate films-Part 2: A numerical experiment. Corrosion, 59(6), 489-497.

[53] Nordsveen, M., Nešic, S., Nyborg, R., & Stangeland, A. (2003). A mechanistic model for carbon dioxide corrosion of mild steel in the presence of protective iron carbonate films-Part 1: Theory and verification. Corrosion, 59(5), 443-456. Chicago

[54] Oelkers, E. H. (1996). Physical and chemical properties of rocks and fluids for chemical mass transport calculations. Reviews in Mineralogy and Geochemistry, 34(1), 131-191.

[55] O'Toole, G., Kaplan, H. B., & Kolter, R. (2000). Biofilm formation as microbial development. Annual Reviews in Microbiology, 54(1), 49-79.

[56] Pak, C. Y., Eanes, E. D., & Ruskin, B. (1971). Spontaneous precipitation of brushite in urine: evidence that brushite is the nidus of renal stones originating as calcium phosphate. Proceedings of the National Academy of Sciences, 68(7), 1456-1460.

[57] Palmer, J., Flint, S., & Brooks, J. (2007). Bacterial cell attachment, the beginning of a biofilm. Journal of industrial microbiology & biotechnology, 34(9), 577-588.

[58] Paraska, D. W., Hipsey, M. R., & Salmon, S. U. (2014). Sediment diagenesis models: Review of approaches, challenges and opportunities. Environmental Modelling & Software, 61, 297-325.

[59] Paz-García, J. M., Johannesson, B., Ottosen, L. M., Ribeiro, A. B., & Rodríguez-Maroto, J. M. (2013). Computing multi-species chemical equilibrium with an algorithm based on the reaction extents. Computers & Chemical Engineering, 58, 135-143.

[60] Pérez, J., Picioreanu, C., & van Loosdrecht, M. (2005). Modeling biofilm and floc diffusion processes based on analytical solution of reaction-diffusion equations. Water research, 39(7), 1311-1323.

[61] Picioreanu, C., van Loosdrecht, M. C., & Heijnen, J. J. (2001). Two-dimensional model of biofilm detachment caused by internal stress from liquid flow. Biotechnology & Bioengineering, 72(2), 205-218.

[62] Pinder, G. F., & Celia, M. A. (2006). Subsurface hydrology. John Wiley & Sons.

[63] Pintelon, T. R., Picioreanu, C., van Loosdrecht, M., & Johns, M. L. (2012). The effect of biofilm permeability on bio-clogging of porous media. Biotechnology and bioengineering, 109(4), 1031-1042.

[64] Pitonzo, B. J., Castro, P., Amy, P. S., Southam, G., Jones, D. A., & Ringelberg, D. (2004). Microbiologically influenced corrosion capability of bacteria isolated from Yucca Mountain. Corrosion, 60(1), 64-74.

[65] Pons, L., Délia, M. L., Basséguy, R., & Bergel, A. (2011). Effect of the semi-conductive properties of the passive layer on the current provided by stainless steel microbial cathodes. Electrochimica Acta, 56(6), 2682-2688.

[66] Prommer, H., Barry, D. A., & Zheng, C. (2003). MODFLOW/MT3DMS-Based Reactive Multicomponent Transport Modeling. Groundwater, 41(2), 247-257.

[67] Reichel, T., Ivanova, L. K., Beaven, R. P., & Haarstrick, A. (2007). Modeling decomposition of MSW in a consolidating anaerobic reactor. Environmental Engineering Science, 24(8), 1072-1083.

[68] Rittman, B. E. (1982). The effect of shear stress on biofilm loss rate. Biotechnology and Bioengineering, 24(2), 501-506.

[69] Qin, C.Z. and Hassanizadeh, S.M. (2015). Reactive Transport and biofilm growth in Porous Media: Pore-Network 1 Modelling. In review.

[70] Schäfer, D., Schäfer, W., & Kinzelbach, W. (1998). Simulation of reactive processes related to biodegradation in aquifers: 1. Structure of the three-dimensional reactive transport model. Journal of contaminant Hydrology, 31(1), 167-186.

[71] Schäfer, D., Schäfer, W., & Kinzelbach, W. (1998). Simulation of reactive processes related to biodegradation in aquifers: 2. Model application to a column study on organic carbon degradation. Journal of Contaminant Hydrology, 31(1), 187-209.

[72] Shaw, M., & Schy, A. (1981). Diffusion coefficient measurement by the" stop-flow" method in a 5% collagen gel. Biophysical journal, 34(3), 375-381.

[73] Steefel, C. I. (2008). Geochemical kinetics and transport. In Kinetics of Water-Rock Interaction (pp. 545-589). Springer New York.

[74] Stewart, T. L., & Fogler, H. S. (2001). Biomass plug development and propagation in porous media.

[75] Støren, T., Simonsen, A., Løkberg, O. J., Lindmo, T., Svaasand, L. O., & Røyset, A. (2003). Measurement of dye diffusion in agar gel by use of low-coher ence interferometry. Optics letters, 28(14), 1215-1217.

[76] Sun, W., Nešic, S., Young, D., & Woollam, R. C. (2008). Equilibrium expressions related to the solubility of the sour corrosion product mackinawite. Industrial & Engineering Chemistry Research, 47(5), 1738-1742.

[77] Usher, K. M., Kaksonen, A. H., Cole, I., & Marney, D. (2014). Critical review: Microbially influenced corrosion of buried carbon steel pipes. International Biodeterioration & Biodegradation, 93, 84-106.

[78] Valencia-Cantero, E., Peña-Cabriales, J. J., & Martínez-Romero, E. (2003). The corrosion effects of sulfate- and ferric-reducing bacterial consortia on steel. Geomicrobiology Journal, 20(2), 157-169.

[79] Van Cappellen, P., & Gaillard, J. F. (1996). Biogeochemical dynamics in aquatic sediments. Reviews in mineralogy and geochemistry, 34(1), 335-376.

[80] Van Cappellen, P., & Wang, Y. (1996). Cycling of iron and manganese in surface sediments; a general theory for the coupled transport and reaction of carbon, oxygen, nitrogen, sulfur, iron, and manganese. American Journal of Science, 296(3), 197-243.

[81] van Paassen, L. A., Ghose, R., van der Linden, T. J., van der Star, W. R., & van Loosdrecht, M. C. (2010). Quantifying biomediated ground improvement by ureolysis: large-scale biogrout experiment. Journal of Geotechnical and Geoenvironmental Engineering, 136(12), 1721-1728.

[82] van Turnhout, A. G., Kleerebezem, R., & Heimovaara, T. J. (2015). How to find the optimal mechanistic reaction network describing your data? a gray modeling toolbox developed and applied on municipal solid waste. In review.

[83] Vardon, P., Thomas, H., He, Q., & Shen, S. L. (2010). Recent Developments in Modelling THCM Behaviour of Geoenvironmental Problems. Geoenvironmental Engineering and Geotechnics, (204), 153.

[84] Venzlaff, H., Enning, D., Srinivasan, J., Mayrhofer, K. J., Hassel, A. W., Widdel, F., & Stratmann, M. (2013). Accelerated cathodic reaction in microbial corrosion of iron due to direct electron uptake by sulfate-reducing bacteria. Corrosion Science, 66, 88-96.

[85] Verma, A., & Pruess, K. (1988). Thermohydrological conditions and silica redistribution near high-level nuclear wastes emplaced in saturated geological formations. Journal of Geophysical Research: Solid Earth (1978–2012), 93(B2), 1159-1173.

[86] Videla, H. A., & Herrera, L. K. (2005). Microbiologically influenced corrosion: looking to the future. International microbiology, 8(3), 169.

[87] Walter, A. L., Frind, E. O., Blowes, D. W., Ptacek, C. J., & Molson, J. W. (1994). Modeling of multicomponent reactive transport in groundwater: 1. Model development and evaluation. Water Resources Research, 30(11), 3137-3148.

[88] Wang, Y., & Papenguth, H. W. (2001). Kinetic modeling of microbially-driven redox chemistry of radionuclides in subsurface environments: coupling transport, microbial metabolism and geochemistry. Journal of contaminant hydrology, 47(2), 297-309.

[89] Yavuz Corapcioglu, M., &Haridas, A. (1984). Transport and fate of microorganisms in porous media: a theoretical investigation. Journal of Hydrology, 72(1), 149-169.

[90] Yeh, G.T., Tripathi, V.S., 1989. A critical evaluation of recent developments in hydrogeochemical transport models of reactive multichemical components. Water Resources Research 25 (1), 93–108.

[91] Zhang, D., Zhang, R., Chen, S., & Soll, W. E. (2000). Pore scale study of flow in porous media: Scale dependency, REV, and statistical REV. Geophysical research letters, 27(8), 1195-1198.

A Energy-based stoichiometry derivation

Table A.1: Standard Gibbs energy of formation (Heijnen and Kleerebezem, 1999)

Name	Structure	Phase	G_f^0 /kJ mol^{-1}
Proton	H^+	aq	−39.9
Water	H_2O	aq	−237.2
Ammonium	$NH_4{}^+$	aq	−79.4
Bisulfide	HS^-	aq	12.1
Sulfate	$SO_4{}^{2-}$	aq	−744.6
Bicarbonate	$HCO_3{}^-$	aq	−586.9
Acetate	$C_2H_3O_2{}^-$	aq	−369.4
Biomass	$C_1H_{1.8}O_{0.5}N_{0.2}$	aq	−67.0

In this energy-based stoichiometry derivation method, the first step is the identification of electron donor and acceptor couple in order to establish the catabolic reaction. For sulfate reducing bacteria, the electron donor couple is $C_2H_3O_2{}^-/HCO_3{}^-$ and the electron acceptor couple is $SO_4{}^{2-}/HS^-$. Based upon the balance of the degree of reduction for both electron donor and acceptor, the catabolic reaction can be formulated accordingly, as shown below:

$$C_2H_3O_2^- + SO_4^{2-} \rightarrow HS^- + 2HCO_3^- \tag{A.1}$$

At the operational temperature, the Gibbs energy changes of this catabolic reaction is $\triangle G^{01}_{cat,SRB} = -47.70$ kJ mol $^{-1}$.

The next step is to establish the anabolic reaction according to the carbon and nitrogen source. For a system using acetate and ammonium as carbon and nitrogen sources respectively, the anabolic reaction is:

$$0.525C_2H_3O_2^- + 0.2NH_4^+ + 0.275H^+ \rightarrow C_1H_{1.8}O_{0.5}N_{0.2} + 0.05HCO_3^- + 0.4H_2O \tag{A.2}$$

where the change of Gibbs energy is $\triangle G^{01}_{ana,SRB} = 29.56$ kJ mol^{-1}.

Despite its generality, the other advantage of this energy-based stoichiometry derivation method is that the catabolic reaction and anabolic reaction can be coupled into an overall reaction. Unlike other solutions which separate the catabolic reaction into half reduction and half oxidation reaction and apply yield coefficient to couple the catabolic reaction with the anabolic reaction, this method greatly reduces the amount of reactions needed for the definition of the microbial growth system and the mass balance conservations are much more clear. To couple the catabolic reaction with the anabolic reaction, the Gibbs energy dissipation per mole biomass

formed needs to be estimated from the carbon length and the degree of reduction of the carbon source using Equation A.3.

$$-\triangle G^{min}_{Overall} = 200 + 18 \times (6 - NoC_{Cs})^{1.8} + exp\{((3.8 - \gamma_{Cs})^2)^{0.16} \times (3.6 + 0.4 \times NoC_{Cs})\} \tag{A.3}$$

where NoC_{Cs} denotes the carbon length of carbon source; γ_{Cs} is the degree of reduction of the carbon source and $\triangle G^{min}_{Overall}$ is the minimum Gibbs energy of dissipation value for the formation of biomass. For a system which has acetate as carbon source, the value for NoC_{Cs} and γ_{Cs} are 2 and 4 respectively. Hence, the estimated Gibbs energy dissipation is $\triangle G^{min}_{Overall} = -432.12$ kJ mol^{-1}.

The catabolic and anabolic reactions are linked via the term catabolism multiplication factor, f_{cat}. The calculation of f_{cat} follows Equation A.4.

$$f_{cat} = \frac{\triangle G^{min}_{Overall} - \triangle G_{ana}}{\triangle G_{cat}} \tag{A.4}$$

The overall reactions is defined as:

$$Overall reaction = Anabolism + f_{cat} Catabolism \tag{A.5}$$

The f_{cat} for this example is calculated as 9.679. The overall reaction is presented as:

$$10.204 C_2H_3O_2^- + 0.2 NH_4^+ + 9.679 SO_4^{2-} + 0.275 H^+ \rightarrow C_1H_{1.8}O_{0.5}N_{0.2} + 19.408 HCO_3^- + 9.679 HS^- + 0.4 H_2O \tag{A.6}$$

After the determination of the stoichiometry for the overall reaction, the biomass yield coefficient can be back calculated via Equation A.7 accordingly.

$$f_{cat} = -\frac{1}{Y^{ogr}} + Y^{an}_D \tag{A.7}$$

where Y^{ogr} is the biomass yield coefficient and Y^{an}_D is the stoichiometry of the electron donor in anabolism. The corresponding biomass yield coefficient for this example is 0.098 mol cell-C/mol OC, which means the microorganisms using 1 mol organic carbon to construct 0.098 mol biomass.

B Gas formation and transfer

Normally, in reactive transport models (Hunter et al., 1998; Schäfer et al., 1998; Walter et al., 1995; Islam and Singhal, 2002), the porous transport medium is assumed to be fully saturated. Without the inclusion of biomass formation, this assumption generally is valid. Metabolism of bacteria is always associated with gas formation. With the presence of bacteria, the void occupied by liquid can vary from 100% to the value approaching zero (Pinder and Celia, 2006). Under this circumstance, the saturation status of the transport medium needed to be considered. The effects of the fully saturation assumption are still relatively unknown. Based upon current investigation, the gas formation might affect the availability of substrates due to the fact that gaseous components are assumed to be excluded from kinetic reactions. The inclusion of gas formation also has influences on the properties of porous medium. Gas formed inside pores could possibly result the partial pressure build-up and induce the detachment of formed biofilm (Gião et al., 2005), and alter the properties of porous medium. In terms of further extensions, two possible solutions regarding the inclusion of gas formation are proposed.

B.1 Pre-defined gas bubble solution

This solution takes the advantages of the nature of biomass formation. If the gas formation is inevitable, it is reasonable to preserve the gaseous volume in the system in advance. A schematic representation of this configuration in REV scale is shown in Figure B.1.

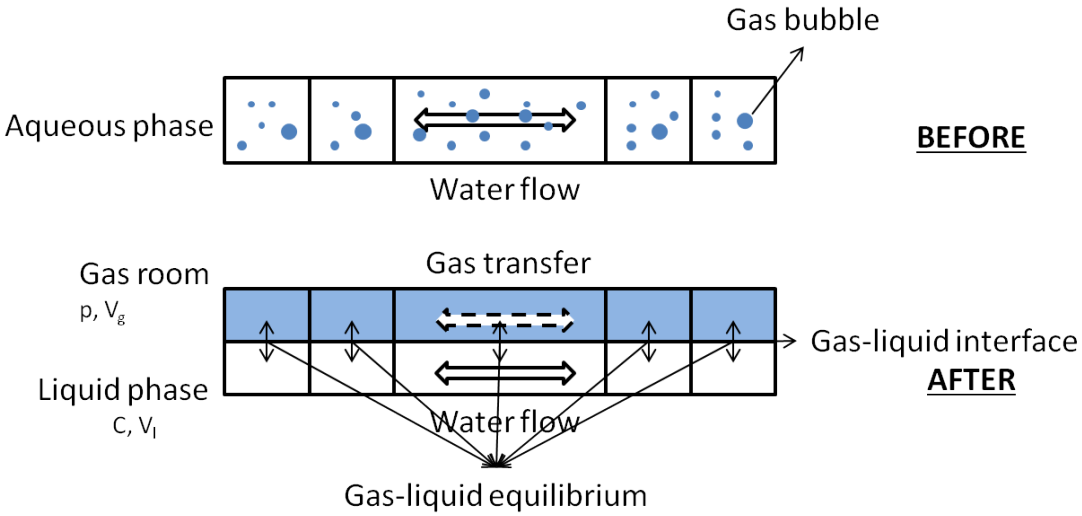


Figure B.1: Schematic representation of gas bubble in the system

This solution sets the gas volume and gas pressure as constant, homogenous and interconnected. The mas balance for gaseous component *i* is expressed as Equation B.1.

$$R_{i,in} = -k_{La,i} \cdot \left(\frac{C_{g,i} \cdot R \cdot T}{V_g \cdot H_i} - C_i \right) \cdot V_l \tag{B.1}$$

$$F_{out} = \sum_{i=1}^{n} R_{i,in} \tag{B.2}$$

$$\frac{dC_{g,i}}{dt} = R_{i,in} - x_i \cdot F_{out} \tag{B.3}$$

where $R_{i,in}$ is the supply of gas i from liquid phase; n is the number of gas component; $k_{La,i}$ is gas transfer rate for gas component i; $C_{g,i}$ is the gas concentration of component i; R is the gas constant; T is the temperature; V_g is the gas volume; H_i is the Henry's coefficient for component i; C_i is the concentration of component i in liquid phase; V_l is the volume of liquid phase; F_{out} represents the amount of gas component i has been collected and x_i is the mass fraction of gas i.

According to Henry's law, the solubility of a gas at fixed temperature in a particular solvent is just a function of the partial pressure of that gas. Equation B.4 gives Henry's law.

$$C_i = H_i P_{gas} \tag{B.4}$$

This solution successfully represents the gas formation process and gas-liquid equilibrium. However, the judgment criteria of gas generation is lacking. As a consequence, the gas bubble always exists and keeps constant. In fact, the formation of gas is subjected to conditions and it is a dynamic process. In addition, the gas partial pressure is set as constant which implies it is impossible to track the gas pressure build-up.

B.2 Unsaturated transport solution

This solution directly treats porous medium as unsaturated transport medium.

The mass balance for water in unsaturated zone is:

$$\Phi S_w P_w \beta_w \frac{\partial P_w}{\partial t} + \Phi \rho_w \frac{\partial S_w}{\partial P_c} \cdot \left(\frac{\partial P_a}{\partial t} - \frac{\partial P_w}{\partial t} \right) - \nabla \cdot \left(\rho_w \frac{k k_{rw}(S_w)}{\mu_w} (\nabla P_w - \rho_w g) \right) = \rho_w Q^w \tag{B.5}$$

Similarly, the mass balance for gas is:

$$P_a \Phi \beta_a \frac{\partial P_a}{\partial t} - \Phi S_w P_a \beta_a \frac{\partial P_a}{\partial t} - \Phi \rho_a \frac{\partial S_w}{\partial t} - \nabla \cdot \left(\rho_a \frac{k k_{ra}(S_w)}{\mu_a} (\nabla P_a - \rho_a g) \right) = \rho_a Q^a \tag{B.6}$$

where $\rho_a Q^a$ expresses the sink term relating to bio/chemical reactions and gas transfer. When the transport medium is fully saturated, Equation B.6 is identical to 0. The judgment criteria for saturated/unsaturated condition is defined by P_c which is calculated from Equation **??**. When $P_c > 0$, it is unsaturated with gas formation, otherwise it is saturated with no gas.

This solution might increase the instability of the numerical simulation significantly. For instance, the calculation of $\partial P_a/\partial t$ and P_a from MATLAB-ORCHESTRA module is questionable. In order to calculate the partial pressure from ORCHESTRA, the gas volume must be defined beforehand. However, this pre-defined gas volume is contradictory with the gas generation judgment criteria which is considered as the main advantage of this unsaturated solution. Hence, the necessities of this solution is doubtful unless a more comprehensive governing equation is proposed.